Jupiter Thermospheric General Circulation Model (JTGCM): Global structure and dynamics driven by auroral and Joule heating

S. W. Bougher, J. H. Waite Jr., and T. Majeed
Space Physics Research Laboratory, University of Michigan, Ann Arbor, Michigan, USA

G. R. Gladstone
Southwest Research Institute, San Antonio, Texas, USA

Received 22 December 2003; revised 7 February 2005; accepted 21 February 2005; published 13 April 2005.

[1] A growing multispectral database plus recent Galileo descent measurements are being used to construct a self-consistent picture of the Jupiter thermosphere/ionosphere system. The proper characterization of Jupiter's upper atmosphere, embedded ionosphere, and auroral features requires the examination of underlying processes, including the feedbacks of energetics, neutral-ion dynamics, composition, and magnetospheric coupling. A fully 3-D Jupiter Thermospheric General Circulation Model (JTGCM) has been developed and exercised to address global temperatures, three-component neutral winds, and neutral-ion species distributions. The domain of this JTGCM extends from 20-μbar (capturing hydrocarbon cooling) to 1.0×10^{-4} nbar (including auroral/Joule heating processes). The resulting JTGCM has been fully spun-up and integrated for $\geq$40 Jupiter rotations. Results from three JTGCM cases incorporating moderate auroral heating, ion drag, and moderate to strong Joule heating processes are presented. The neutral horizontal winds at ionospheric heights vary from 0.5 km/s to 1.2 km/s, atomic hydrogen is transported equatorward, and auroral exospheric temperatures range from $\sim$1200–1300 K to above 3000 K, depending on the magnitude of Joule heating. The equatorial temperature profiles from the JTGCM are compared with the measured temperature structure from the Galileo ASI data set. The best fit to the Galileo data implies that the major energy source for maintaining the equatorial temperatures is due to dynamical heating induced by the low-latitude convergence of the high-latitude-driven thermospheric circulation. Overall, the Jupiter thermosphere/ionosphere system is highly variable and is shown to be strongly dependent on magnetospheric coupling which regulates Joule heating.

Citation: Bougher, S. W., J. H. Waite Jr., T. Majeed, and G. R. Gladstone (2005), Jupiter Thermospheric General Circulation Model (JTGCM): Global structure and dynamics driven by auroral and Joule heating, *J. Geophys. Res.*, *110*, E04008, doi:10.1029/2003JE002230.

1. Why Address Jupiter Thermospheric Energetics and Dynamics?

1.1. Introduction

[2] The long-term objective of our program in comparative planetary atmospheres is to contrast and compare the physical and chemical processes responsible for the structure and dynamics of the thermospheres of Venus, Earth, Mars and Titan (terrestrial-like planets and moons) plus Jupiter and Saturn (Jovian-like planets). Fundamental planetary parameters for these bodies are sufficiently unique to provide independent "laboratories" to examine the changing roles of various thermospheric processes controlling their energetics, dynamics, and composition. Recently, three-dimensional (3-D) Thermospheric General Circulation Models (TGCMs) for Venus, Earth, and Mars were exercised to examine the seasonal-solar cycle responses of each of these upper atmospheres [*Bougher et al.*, 1999, 2000]. Intercomparisons have illustrated the key roles of time-varying energy deposition, IR cooling, and dynamics in controlling their global thermospheric structures. Various multispectral data sets and the Galileo probe descent measurements are now available for Jupiter, motivating us to extend this basic TGCM formulation to address the role of auroral plus Joule heating processes for determining the Jovian thermospheric structure and dynamics.

[3] The development and exercising of such a Jupiter TGCM is required to compare the thermosphere/ionosphere structures and dynamics of those planets having significant

Copyright 2005 by the American Geophysical Union.
0148-0227/05/2003JE002230

intrinsic magnetic fields (e.g., Earth and Jupiter). Clearly, a strong link exists between the strength of a planetary magnetic field and its mean and time-variable thermospheric temperature distribution and global winds. For example, the Earth's upper atmosphere is subject to episodic (magnetic storm period) forcing due to strong auroral processes that result from its significant intrinsic magnetic field and its interaction with the solar wind. Combined auroral plus Joule heating yields a global power input of nearly $0.8-5 \times 10^{11}$ W, which strongly modifies the global thermospheric circulation pattern. By comparison, auroral plus Joule heating is expected to be nearly $1000\times$ larger for Jupiter than for Earth during typical storm conditions [*Strobel*, 2002]. Jupiter's auroral and Joule heating processes are generally thought to be powered by the planet's internal rotation [cf. *Waite and Lummerzheim*, 2002]. As a result of this, and the factor of 25 decrease in solar forcing compared to Earth, Jupiter's thermospheric structure and dynamics are expected to be dominated by its auroral and Joule heating processes at all times over the entire globe [e.g., *Waite et al.*, 1983; *Strobel*, 2002].

1.2. Brief Review of Multispectral and Galileo ASI Data

[4] Remote sensing of Jupiter's aurora from X-ray to radio wavelengths has revealed much about the nature of the Jovian aurora and about the impact of the ionosphere-magnetosphere coupling on the thermal balance and dynamical drivers of the upper atmosphere of Jupiter (see review by *Waite et al.* [2000]). For example, the combination of X-ray and ultraviolet measurements indicate that both energetic heavy ions and electrons energized in the middle and outer magnetosphere contribute to auroral excitation. Despite the fact that no in situ measurements exist for the neutral atmosphere of Jupiter's auroral region, H_3^+ near-infrared spectra in the pressure range of 10^{-6} to 10^{-10} bars indicate auroral exospheric temperatures >1200 K [e.g., *Drossart et al.*, 1989; *Miller et al.*, 1990; *Lam et al.*, 1997; *Stallard et al.*, 2002; *Raynaud et al.*, 2004], consistent with recent calculations based on a 1-D auroral energy transport model [*Grodent and Gérard*, 2001] and an available 3-D general circulation model [*Millward et al.*, 2002].

[5] Recently, high-resolution H_3^+ observations were used to obtain information on the Jovian upper atmosphere ion winds in addition to the temperature and column density. *Rego et al.* [1999] detected doppler shifted H_3^+ emission lines from the northern auroral regions using the NASA Infrared Telescope Facility (IRTF) high-resolution spectrometer, CSHELL. Their measurements showed an anticorotational ion wind with a velocity of >2 km/s. Using the same instruments, *Stallard et al.* [2001] measured the H_3^+ winds across the northern polar region to be somewhat weaker in magnitude (1.2–1.5 km/s). This observed H_3^+ electrojet flows counter to the planetary rotation around the main auroral oval, thereby confirming the initial Rego et al. detection. It is noteworthy that the sound speed at thermospheric altitudes is 2–3 km/s. The mechanism for accelerating these ions (and electrons) focuses on corotation breakdown of magnetospheric plasma [e.g., *Hill*, 1979, 2001; *Cowley and Bunce*, 2001]. In short, localized ion winds up to a few km/s have been observed, demonstrating the tremendous atmospheric response to strong magnetosphere-ionosphere coupling on very short timescales.

[6] Conversely, the Atmospheric Structure Instrument (ASI) on the Galileo probe [cf. *Seiff et al.*, 1998] provided the first in situ measurements of Jupiter's neutral atmospheric structure from 1029 km to 133 km (altitudes are referenced to 1 bar pressure level) near the Jovian equator (Lat: 6.5; λ_{III}: 4.5). The λ_{III}(1965) coordinate system is defined by *Dessler* [1983]. The derived temperature profile exhibited wave-like variations and increases from ~200 K at 400 km altitude to about 950 K at 1000 km altitude. This temperature structure is consistent with that inferred from previous solar and stellar occultation experiments during the Voyager flybys in 1979, as reanalyzed recently by *Yelle et al.* [1996]. The periodic temperature variations in the ASI profile have been interpreted as being due to upward propagating gravity waves [*Young et al.*, 1997; *Matcheva and Strobel*, 1999; *Hickey et al.*, 2000]. It has been suggested that gravity waves may not be sufficient to heat the Jovian thermosphere to observed temperatures. Instead, the net heating in the equatorial upper atmosphere may be due to other processes such as charged particle precipitation [*Waite et al.*, 1997] and transport resulting from adiabatic heating induced by the downward vertical motion of the aurorally driven thermospheric circulation [*Waite et al.*, 1983]. In particular, ROSAT observations have revealed soft X-ray emissions from Jupiter's lower latitudes as well as from the auroral zones, implying that energetic particle precipitation also occurs at low latitudes in regions linked to the inner radiation belts [*Waite et al.*, 1997].

[7] Recent coincident observations of the Jovian environment by Hubble Space Telescope (HST), Chandra X-ray Observatory (CXO), Cassini and Galileo spacecraft during the period from 14 December 2000 to 21 January 2001 provide a unique opportunity to understand the complex nature of physical processes that control the dynamics of the coupled ionosphere-magnetosphere system and its interaction with the solar wind. Comparisons of auroral ultraviolet (UV) images [*Grodent et al.*, 2003] and event maps of the Jovian X-ray aurora [*Waite et al.*, 2001; *Gladstone et al.*, 2002] have identified new morphological features, their variations with time, and the energetics of the polar emissions, suggesting that their source is magnetically connected to the outer regions of Jupiter's magnetosphere. On the other hand, the source of fast ionospheric winds and auroral heating at Jupiter's main auroral oval have been linked to the breakdown in the equatorial plasmasheet corotation between 20 and 30 R_J where large field-aligned currents are generated [cf. *Cowley and Bunce*, 2001; *Waite and Lummerzheim*, 2002]. Thus the variability of Jupiter's thermospheric dynamics is likely driven by its own magnetosphere acting through a corotational electric field.

1.3. Implications of Jovian Thermospheric Dynamics

[8] Strong auroral plus Joule heating concentrated in the auroral oval regions of both Jovian hemispheres likely provides forcing that drives strong meridional flow that is subject to the Coriolis torques consistent with a rapidly rotating planet; i.e., equatorial winds are turned westward (anticorotation direction) by these Coriolis torques. The model calculations of *Sommeria et al.* [1995] are quite controversial and have shown that an extremely rapid (in

excess of 20 km/s) auroral electrojet can generate neutral winds up to 20 km/s. Such supersonic winds could disperse high-latitude heating globally through a strong equatorward flow thereby explaining high Jovian exospheric temperatures at low latitudes. However, there is no observational evidence to date to support winds of such large magnitudes. Rather, recently measured electrojet winds of 1–2 km/s [*Rego et al.*, 1999; *Stallard et al.*, 2001] suggest neutral winds of the order of ~1 km/s. The ability of such strong (yet subsonic) horizontal winds to overcome Coriolis torques needs to be addressed in the context of a global circulation model (see section 3.1). In addition, global redistribution of atomic hydrogen from the high-latitude thermosphere may be possible in response to transport by these same strong meridional winds. Because atomic hydrogen is a minor constituent of the Jupiter thermosphere and is relatively easy to monitor by remote sensing of the H Lyman-α line, it can serve as a very useful tracer of the Jovian thermospheric winds (see sections 3.2 and 4).

[9] The Jovian Ionospheric Model (JIM) developed by *Achilleos et al.* [1998] is the first 3-D coupled ionosphere-thermosphere model which demonstrated that some of the energy deposited by high-latitude processes in the auroral regions can be transported to the Jovian equator by the meridional component of the thermospheric circulation. *Millward et al.* [2002] have recently modified JIM and calculated an equatorial temperature profile near local noon with an exospheric temperature of 1200 K.

1.4. Objectives of This Paper

[10] In this first paper, we present details regarding the formulation, development, and testing of the Jupiter Thermospheric General Circulation Model (JTGCM) plus interpretation of initial JTGCM production runs. A second paper presents the detailed results from the JTGCM focused on equatorial temperatures and their comparison with Galileo probe data (T. Majeed et al., Processes of equatorial thermal structure: An analysis of a Galileo temperature profile with a 3-D model, submitted to *Journal of Geophysical Research*, 2004; hereinafter referred to as Majeed et al., submitted manuscript, 2004). The JTGCM is being used to simulate the high-speed thermospheric winds along with global temperature and ion-neutral species distributions. The main goals of our present JTGCM model investigations are as follows: (1) to demonstrate the role of aurora plus Joule heating processes in controlling the thermospheric structure and the time-variable character of the global wind system; (2) to provide an initial analysis of the dynamical heating mechanism(s) for maintaining ~1000 K equatorial temperatures; (3) to quantify the role of global winds in redistributing atomic hydrogen about the planet, and to potentially identify a mechanism for generating an equatorial bulge; and finally (4) to characterize the relative roles of ion drag and Joule heating in driving neutral thermospheric winds and the associated mapping of these drivers into the magnetosphere.

[11] Three simulations from the newly developed JTGCM are specifically presented in this paper: (1) a simplified case incorporating moderate auroral forcing alone; (2) a coupled case incorporating auroral forcing, reduced (30%) ion drag, plus the associated Joule heating, and (3) a coupled case incorporating auroral, full (100%) ion drag, plus Joule heating. Each of these JTGCM cases is analyzed using postprocessor diagnostic and plotting routines available for detailed studies.

[12] The organization of this paper is briefly outlined. Section 2 provides details regarding the framework, physical parameterizations, and inputs constituting the JTGCM code itself. Section 3 illustrates key JTGCM model outputs for three cases that have been selected to represent plausible Jovian upper atmosphere conditions. Equatorial thermal balances required to approximate the Galileo ASI temperature profile are given for Case 2; similar polar thermal balances corresponding to this 30% Joule heating simulation are also given. Section 4 provides JTGCM diagnostic quantities that link the present simulations with available observational constraints. Section 5 provides initial comparisons of Case 2 outputs to corresponding JIM model simulations. Finally, section 6 concludes and points to future planned upgrades for the JTGCM code.

2. Jupiter Three-Dimensional Model Formulation and Inputs

2.1. JTGCM Overview

[13] The JTGCM is a finite difference primitive equation model that solves for neutral temperatures, neutral-ion densities, and three component neutral winds over the globe. Full self-consistency among the key energetic, chemical, and dynamical processes affecting the Jovian upper atmosphere is the eventual goal for this JTGCM code. The framework and results presented in this paper demonstrate a significant step in this direction. A fourth-order center-difference formulation is used, similar to that employed for planetary TGCMs for Venus, Earth, and Mars [e.g., *Bougher et al.*, 1999, 2002]. Prognostic equations for the major neutral species (H_2, He, and H) and several key ions (e.g., H_3^+, H^+, H_2^+) are included. Minor hydrocarbon (C_2H_2 and CH_4) densities are specified at/below the homopause on the basis of offline detailed photochemical model calculations by *Gladstone et al.* [1996]. Future minor species will include H_2 vibrational states (ν = 1–4) required to calculate H^+ chemical losses explicitly. At present, H^+ ions are prescribed on the basis of the offline 1-D model calculations of *Waite et al.* [1983]. The remaining ions (H_3^+ and H_2^+) are calculated assuming photochemical equilibrium conditions. Zonal, meridional, and vertical velocities, total temperatures, and geopotential heights are also obtained on 39-pressure levels (above 20.0 μbar), corresponding to ~250–3000 km above the 1 bar reference pressure level with a 5° latitude and longitude resolution. The vertical coordinate is log-pressure, with a vertical spacing of two grid points per scale height. The maximum eddy coefficient (K_{zz}) for eddy transport (diffusion and viscosity) is easily adjusted; i.e., presently, it is specified (~2×10^{10} m^2/s) to properly locate the CH_4 homopause near 4.5-μbar.

[14] The JTGCM was developed from a suitable adaptation of the NCAR Thermosphere Ionosphere General Circulation Model (TIGCM) [*Roble and Ridley*, 1987; *Roble et al.*, 1988]. The same primitive equation set is employed in a finite difference framework for the JTGCM code. The TIGCM dynamical core is retained, along with the general solvers utilized for the major and minor species

Table 1. Jupiter Fundamental Parameters

Parameter	Value
Gravity, m/s^2	24.50
Heliocentric distance, AU	5.2
Radius, km	71400
Ω, rad/s	1.76×10^{-4}
Day, Earth seconds	35730
Magnetic dipole moment (wrt Earth)	10–15
Ref. pressure (p0), μbar	4.5
Max. eddy diff. coeff., m^2/s	2.0×10^{10}

(including diffusion and advection), and the energy equation. However, significant changes in model inputs and physics were made to effectively modify the terrestrial physics to the environment of Jupiter. In particular, hydrocarbon and H_3^+ cooling (section 2.4), simplified gas giant ion-neutral chemistry (section 2.5), and production functions for key ions and neutrals (section 2.5) are incorporated. Most importantly, the JTGCM makes use of Jupiter specific parameterizations for auroral forcing, ion drag, and Joule heating processes (see sections 2.6–2.8). JTGCM model results will be shown to depend critically on these thermal and dynamical drivers. In addition, the domain of the JTGCM extends from 20-μbar (to capture the bulk of hydrocarbon cooling) to 1.0×10^{-4} nbar (sufficient to include most auroral plus Joule heating processes and the corresponding winds).

[15] Fundamental parameters that are unique to Jupiter and specified within the JTGCM are outlined in Table 1. The fast planetary rotation immediately implies that Coriolis torques will strongly impact the global thermospheric wind system. In addition, the heliocentric distance at Jupiter is sufficiently large to render solar EUV heating inadequate to account for the observed thermospheric temperatures [e.g., *Strobel and Smith*, 1973; *Strobel*, 2002]. The large Jupiter gravity, small mean molecular weights of atomic and molecular hydrogen and helium, and warm thermospheric temperatures combine to give rise to large scale heights (up to 100–300 km) for the major species (H_2, He, and H). Finally, the presence of a significant intrinsic magnetic field (approximately 10–15 Gauss at the surface at auroral latitudes) implies that auroral, ion drag, and Joule heating processes are very important, similar to the Earth during magnetic storm conditions.

[16] Figure 1 summarizes the various thermosphere/ionosphere/magnetosphere processes that are presently (or planned to be) incorporated into the JTGCM code. The color coding indicates the time evolution of the JTGCM code development, some early assumptions made, and the increasing complexity of coupled processes as model stages are completed. The color coding also corresponds to the three cases to be presented in this paper. For all JTGCM cases, auroral forcing is prescribed to be symmetric in $\lambda_{III(1965)}$ longitude [*Dessler*, 1983] about empirically specified north

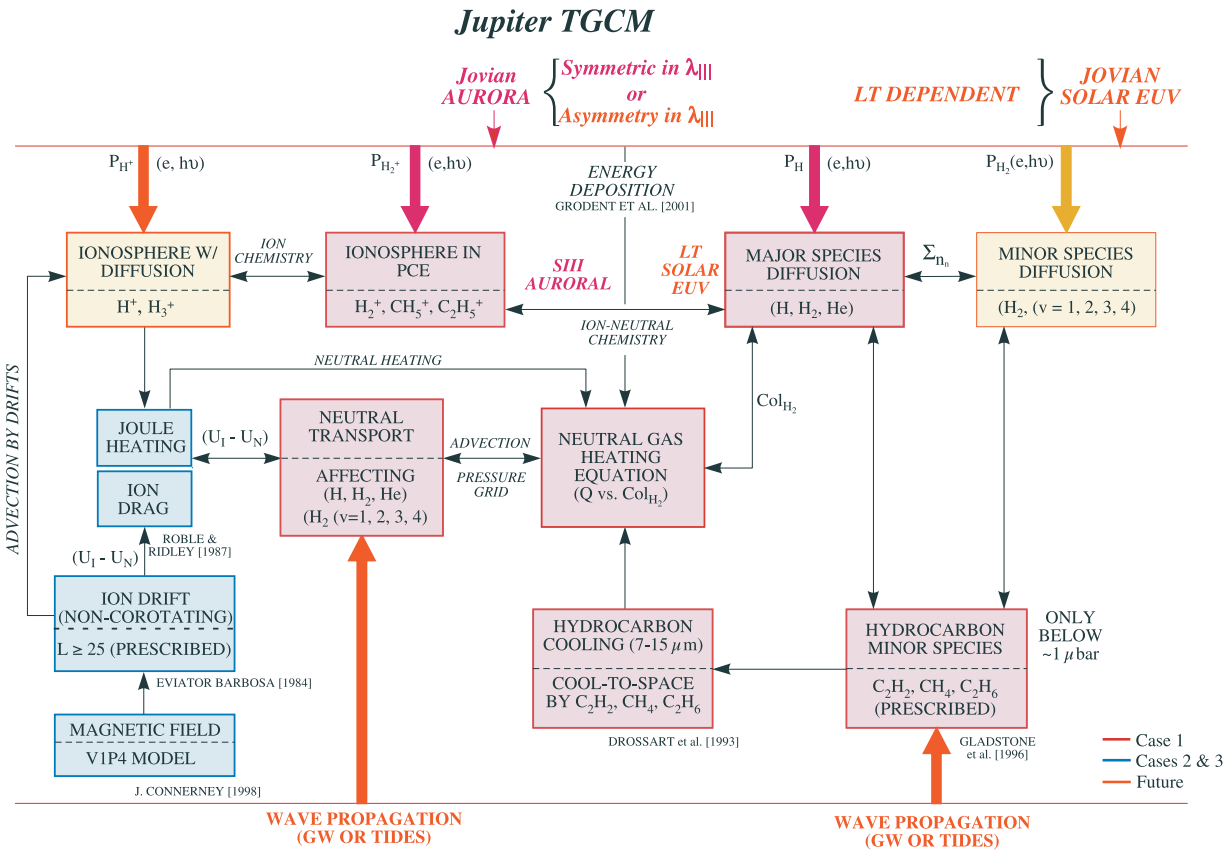

Figure 1. Jupiter TGCM overview. This schematic summarizes the various thermosphere/ionosphere/magnetosphere processes and their couplings that are presently incorporated into the JTGCM code. Case 1, 2, and 3 processes are identified corresponding to JTGCM simulations presented in this paper. Future planned upgrades and processes are also indicated.

and south auroral ovals (see section 2.6). Jovian solar EUV heating is neglected at this stage of JTGCM code development, since both auroral and Joule heating components are estimated to be at least 100 times greater [e.g., *Strobel*, 2002]. Auroral electron precipitation sources of H and H_2^+ are important to incorporate into the JTGCM code; this is accomplished using parameterized production functions taken from the detailed 1-D photochemical/diffusion model of *Waite et al.* [1983] (see section 2.5). Ion-neutral chemical sources of H are also included in its production function. However, solar photo-electron contributions to these sources of H and H_2^+ are presently neglected. Likewise, auroral electron heating is parameterized according to the 1-D model of *Grodent and Gérard* [2001] (see details in section 2.6). This auroral heating function incorporates exothermic chemical heating. All JTGCM cases include the solution of the coupled continuity-diffusion equations for the major species (H_2, He, and H) along with their transport by the large-scale thermospheric circulation. Hydrocarbon cooling (section 2.4) is incorporated making use of prescribed densities of C_2H_2, C_2H_6 and CH_4; also H_3^+ cooling (3–4 microns) is included above the homopause. Finally, a photochemical ionosphere is constructed to address the major ions (H_3^+ and H_2^+), assuming that chemical time scales are short compared to local dynamics (see section 2.5). This assumption is fine for H_2^+ and H_3^+, but not for H^+ [*Millward et al.*, 2002]. Instead, H^+ is presently prescribed within the JTGCM on the basis of the 1-D model formulation of *Waite et al.* [1983]. This scheme does not include H_2 vibrational states as a sink for H^+ ions (see details in section 2.5).

[17] Of our three JTGCM simulations (see 1.4), Case 1 considers high-latitude auroral (electron precipitation) plus equatorial drizzle (ion precipitation) heating and the corresponding impacts on the thermal and dynamical structure (see section 2.6). For Cases 2 and 3, a detailed Jupiter magnetic field model (VIP4) is incorporated (see section 2.7). A magnetosphere model is also adopted from Voyager observations, enabling a convection electric field and corresponding ion drift pattern to be calculated (see section 2.8). This leads to the calculation of conductivities and ion drag forcing terms for the momentum equations. The corresponding Joule heating pattern is combined with the precipitation-driven auroral heating pattern already calculated. Case 2 assumes a 30% efficiency for ion drag and Joule heating; Case 3 assumes a 100% efficiency. Magnetosphere-ionosphere coupling is implicitly incorporated in this mapping of the convection electric field and ion drift patterns out into the magnetosphere.

[18] The JTGCM code is constructed with significant differences from the previous Jovian Ionosphere Model (JIM) described in various publications [e.g., *Achilleos et al.*, 1998; *Millward et al.*, 2002]. Most importantly, the JTGCM code spans a wider pressure range than JIM (2-μbar to 0.02-nbar); this enables hydrocarbon cooling at/below the JTGCM homopause to be incorporated for dissipating auroral and Joule heating. In addition, a more realistic magnetic field model is included in the JTGCM (see section 2.7 describing the VIP4 model); when combined with a Voyager-based ion convection model (section 2.7) empirically motivated ion drag and Joule heating patterns (single cells) are produced around the main auroral ovals in the north and south. These different model features warrant the detailed comparison of JTGCM and JIM simulations for common input parameters. Such studies are beyond the scope of this paper; however, initial comparisons of JTGCM and JIM fields will be made (see section 5).

2.2. Governing Equations

[19] The JTGCM code uses the same basic set of primitive equations found in the TIGCM for the neutrals, i.e., the thermodynamic equation, zonal (U) and meridional (V) momentum equations, the coupled continuity-diffusion equations (now for H and He), the hydrostatic equation, and the continuity equation (yielding vertical velocities) [cf. *Roble et al.*, 1988; *Bougher et al.*, 1988]. The goal here is to apply a consistent suite of primitive equations for the Jupiter thermosphere and ionosphere in order to facilitate JTGCM comparisons with Earth TIGCM outputs. Each of these JTGCM equations is cast in log-pressure coordinates (zp = ln(p0/p)), with a reference pressure level that is specified corresponding approximately to the average homopause level. For the JTGCM code, this reference pressure (p0) is located at 4.5-μbar (zp = 0). Each zp interval corresponds to 0.5-scale height at the local temperature.

[20] For the thermodynamic (energy) equation, incorporated terms include those that capture molecular and eddy conduction, adiabatic heating/cooling, hydrodynamic (horizontal and vertical) advection, the sum of all heating components (auroral plus Joule heating), and all IR cooling components (derived from hydrocarbon and H_3^+ emissions). The momentum equations (zonal and meridional) include terms addressing molecular viscosity, curvature forces, Coriolis forces, hydrodynamic advection, the geopotential gradient force, and ion drag forces. Specific heat at constant pressure (Cp), thermal conductivity (Kt), and molecular viscosity (Km) parameters needed in these equations are calculated on the basis of the *Banks and Kockarts* [1973] gas mixture method and updated H_2 coefficients from *Lide* [1997]. Each of the terms in these three prognostic equations is routinely isolated for comparison using the JTGCM postprocessing diagnostic package (see section 3).

[21] The coupled multiconstituent continuity equations for the three major species (H_2, He, and H) properly account for their mutual diffusion, eddy diffusion, horizontal and vertical advection, and photochemical sources and sinks. A matrix operator is employed to simultaneously solve these three-component continuity-diffusion equations implicitly, thereby speeding the calculation tremendously. Mutual diffusion coefficients (e.g., H-H_2, H-He, H_2-He) are calculated on the basis of tables from *Mason and Marrero* [1970] and updated according to *Atreya* [1986]. The temperature and pressure dependencies for these diffusion coefficients are included using the formulation described by *Banks and Kockarts* [1973]. Thermal diffusion coefficients are also important for these light species (e.g., He-H_2), and are taken from *Chapman and Cowling* [1970]. The time scale for molecular diffusion is calculated to be many (Earth) days near the Jupiter homopause. Mass weighted mixing ratios are ultimately calculated for each specie, in accord with the TIGCM formulation used for Earth, Venus, and Mars. Conversion to number densities (or other units) is accomplished during postprocessing.

[22] A simplified set of neutral-ion chemical equations (see Table 2 and section 2.5) provides the photochemical

Table 2. Simplified JTGCM Ion-Neutral Reactions and Rates[a]

Reactions	Rates	References
$2H + M \rightarrow H_2 + M$	$1.5 \times 10^{-29}/T^{1/3}$	1
$H + CH_4 \rightarrow CH_3 + H_2$	$3.73 \times 10^{-20}T^3\exp(4406/T)$	1
$H + C_2H_2 + M \rightarrow C_2H_3 + M$	$6.4 \times 10^{-25}/T^2\exp(1200/T)$	1
$H_2^+ + H \rightarrow H^+ + H_2$	6.4×10^{-10}	2 or 3
$H_2^+ + H_2 \rightarrow H_3^+ + H$	2.0×10^{-9}	3
$H_2^+ + He \rightarrow HeH^+ + H$	1.4×10^{-10}	3
$H_2^+ + CH_4 \rightarrow CH_5^+ + H$	1.1×10^{-10}	3
$H_2^+ + CH_4 \rightarrow CH_4^+ + H_2$	1.4×10^{-9}	3
$H_2^+ + CH_4 \rightarrow CH_3^+ H + H_2$	2.3×10^{-9}	3
$H^+ + 2H_2 \rightarrow H_3^+ + H_2$	3.2×10^{-29}	3
$H_3^+ + e \rightarrow H_2 + H$	$4.8 \times 10^{-8}(300/Te)^{1/2}$	4
$H_3^+ + e \rightarrow 3H$	$6.2 \times 10^{-8}(300/Te)^{1/2}$	4
$H_3^+ + CH_4 \rightarrow CH_5^+ + H_2$	2.4×10^{-9}	3

[a]References: 1, *Gladstone et al.* [1996]; 2, *Atreya* [1986]; 3, *Kim and Fox* [1994]; 4, *Mitchell et al.* [1983]; *Sundstrom et al.* [1994]. Te and T denote electron and neutral temperatures. M denotes background main neutral species in the lower thermosphere (H_2). Units of rates: 2-body reactions, cm^3/s; 3-body reactions, cm^6/s.

sources and sinks primarily for atomic hydrogen. Molecular hydrogen, the dominant background gas, is calculated as the remainder of the total density after helium and atomic hydrogen are subtracted. These three major species are used to derive the background atmosphere, upon which pressure and geopotential gradients are defined, yielding the net driver for the thermospheric circulation. By definition, minor species have no impact on the mean molecular weight or pressure (and geopotential) gradients within the JTGCM code.

[23] The eddy diffusion coefficient profile used in the JTGCM code is parameterized according to standard aeronomic formulations. A key feature about the JTGCM is that the magnitude of the eddy coefficient is chosen to place the equatorial CH_4 homopause at 4.5-μbar. Presently, the maximum eddy coefficient (K_{zz}) for eddy diffusion and viscosity is 2×10^{10} m^2/s; no latitude or longitude variation is included.

[24] TIGCM modification for Jupiter also requires that we generalize the definition of time within the model to permit any rotational period to be accommodated. Specifically, we adopt "Jupiter time," based on a Jovian day or 24 Jupiter hours (1 rotation), for use in the control code. This is equivalent to redefining the Jupiter second to conform to a 24-hour day like that of the Earth. For these exercises, the length of the Jupiter day is set at 35730 Earth seconds. This transformation enables the JTGCM model runs to be handled with the same bookkeeping scheme used for the Earth TIGCM. Furthermore, it permits the TIGCM interpolation routines to shift correctly the local time through Jovigraphic (λ_{III}) longitude during the course of a JTGCM model rotation. However, for all the dynamical, chemical, and energetic formulations of the JTGCM code, standard Earth seconds are employed. The JTGCM time step is presently set at 60 seconds.

2.3. Boundary Conditions, Steady State, and Filtering

[25] The lower boundary in the JTGCM was chosen at 20 μbars (~250 km above the 1-bar level) to accommodate the peaks of the hydrocarbon cooling layers due to C_2H_2 and CH_4 near the homopause level. In particular, this is important for proper cooling of the Jovian auroral atmosphere where strong electron precipitation provides heating that is conducted downward and radiated away via these strong IR emissions. H_3^+ cooling from IR emissions [*Drossart et al.*, 1989] has also been included above the homopause (see section 2.4). Our assumed boundary conditions are that the geopotential, zonal (U) and meridional (V) winds are zero at the lower boundary (i.e., strict corotation). This is surely a crude simplification that neglects the strong stratospheric winds [e.g., *Flasar et al.*, 2004] and upward propagating tides and gravity waves [e.g., *Young et al.*, 1997; *Matcheva and Strobel*, 1999; *Hickey et al.*, 2000] that must be present in the Jovian lower atmosphere. Global average lower boundary conditions for temperature and neutral densities (H and He) are taken from Galileo [*Seiff et al.*, 1998] and Voyager data [*Festou et al.*, 1981]. Specifically, a globally average temperature, composed of observed equatorial and polar values near 250 km, is set to 190K. The helium volume mixing ratio is set to 0.135 at 250 km on the basis of Galileo probe observations [*Niemann et al.*, 1996]. The atomic hydrogen volume mixing ratio is set to 4.23×10^{-8}, in accord with Voyager data. Photochemical equilibrium is assumed for the major ions (H_3^+ and H_2^+).

[26] Upper boundary conditions were specified at $\sim 1.1 \times 10^{-4}$ nbar in order to properly include the high-altitude auroral heating processes [e.g., *Grodent and Gérard*, 2001]. Corresponding boundary conditions for temperatures and neutral winds are identical to those employed in the terrestrial TIGCM; i.e., vertical gradients in temperatures and winds (zonal, meridional, vertical) are set to zero at the model top. These conditions are in accord with weak energy sources at high altitudes; isothermal temperatures are also consistent with the emergence of the exosphere. For composition (H and He), diffusive equilibrium is assumed at the top boundary. Departures from diffusive equilibrium are driven elsewhere by the hydrodynamic transport terms and the net sources. Atmospheric escape of atomic hydrogen and helium for Jupiter is presumed to be negligible, owing to its strong gravity.

[27] Each of the JTGCM prognostic equations (thermodynamic, 2-momentum, 2-composition) is time dependent, but is typically integrated toward steady-state conditions. Thus each simulation of the JTGCM thermosphere/ionosphere code is allowed to run for 40 to 60 Jovian rotations in order to approach a cyclic steady-state solution in the modeled fields. After this time, calculated temperatures, horizontal and vertical wind velocities and densities (H_2, He, H and major ions) may continue to vary slightly for pressures above the ~1.0 μbar level (below roughly 350 km). This is reflected in thermal energy balances that are calculated above (steady state) and below the CH_4 homopause (see section 4). However, the primary global patterns in the horizontal distributions of these JTGCM calculated fields are clearly stabilized at higher altitudes. Longer integrations are needed to confirm similar steady-state conditions below ~350 km.

[28] Planetary TGCMs achieve steady-state solutions according to various time scales that vary as a function of altitude [e.g., *Bougher et al.*, 1999, 2002]. For Jupiter's thermosphere, a dynamical time scale can be defined as the transport time for average meridional winds to redistribute auroral oval region heat and atomic species to the Jovi-

graphic equator. Typical JTGCM zonal averaged meridional winds (~125 to 300 m/s) place this timescale at ~4–10 Earth days for pressures below about 0.15 μbar. Equilibration requires that meridional pressure gradients are stabilized by both pole-to-equator and equator-to-pole wind flow (i.e., "sloshing"), for which the dynamical timescale should be multiplied by 2. Thus the "effective" dynamical timescale is estimated to be ~8–20 Earth days (or 20–50 Jovian rotations). Hence JTGCM calculations can only achieve near equilibrium solutions when simulations are run on the order of ≥40 Jovian rotations. This requirement makes running JTGCM cases very time consuming when using 60 sec time steps. For this paper, we have appropriately elected to focus on three JTGCM cases only, each of which has been integrated for at least 40-rotations, yielding steady-state solutions. It is interesting that the 1-way dynamical transport timescale (~4–10 Earth days) is comparable to the H_3^+ cooling timescale (~4.5 days) inferred from observations in the main auroral oval [*Lam et al.*, 1997]; the timescale for molecular thermal conduction is also similar. Hence meridional transport, thermal conduction, and H_3^+ cooling are expected to be competing processes in the Jovian upper thermosphere. However, the most important barrier to meridional transport of high-latitude auroral and Joule energy is likely to be the Coriolis force. Dynamical model simulations are required to investigate what magnitude of mean meridional winds is required to overcome this Coriolis force.

[29] The preceding equations using the fourth-order finite-difference computational scheme require that certain filtering, smoothing, and time-step assumptions be invoked to achieve numerical stability [e.g., *Bougher et al.*, 1988]. Filtering of the shorter wavelength, fast-moving waves of the prognostic variables in the polar regions by Fourier analysis prevents linear instability when using the 60 second time step. Hence only low wave number components (≤wave number 6 at 82.5 latitude, and ≤ wave number 2 at 87.5 latitude) of the temperature (T), zonal (U) and meridional (V) wind, and composition fields are retained at high latitudes. This filtering is also important, since grid sizes shrink in spatial extent as the pole is approached. Smoothing, using the frequency filter originally designed by *Robert* [1966], and nonlinear horizontal diffusion are added to the JTGCM prognostic fields to control the time computational mode and nonlinear instabilities. Finally, a simple Rayleigh friction parameterization was employed at the start of JTGCM spin-up in order to control lower boundary instabilities. Later, this artificial friction (dissipation) was removed entirely as molecular and eddy viscosity became important. Use of these filtering, smoothing, and horizontal diffusion schemes does not significantly alter the basic (mean) prognostic fields. However, the appropriate time step is still limited by the horizontal wind speeds achieved in any given JTGCM simulation. For the JTGCM cases presented in this paper, a 60 second time step is completely adequate.

2.4. Hydrocarbon and H_3^+ Cooling Formulations

[30] The lower boundary of the JTGCM code is set at 20-μbar, in order to capture the bulk of the hydrocarbon (HC) cooling due to strong C_2H_2 (12.6-micron) and CH_4 (7.8-micron) emissions at the base of the thermosphere, below the homopause. HC cooling constraints were provided by reanalyzing the Voyager 1 Infrared Interferometer and Radiometer Spectrometer (IRIS) spectra [*Drossart et al.*, 1993]. The total measured excess IR auroral zone emission (average over the IRIS field of view) in the HC bands between 7 and 13 microns was found to be about 208 mW/m^2 over an area of about 2×10^{14} m^2 with a resulting power output of 4×10^{13} W. This large IR output likely results from a large temperature enhancement in the upper stratosphere and lower thermosphere, in accord with strong auroral plus Joule heating that is conducted downward and made available for IR radiation.

[31] The conditions within the Jovian upper atmosphere (p = 1.0 to 1.0×10^{-4} μbar) permit H_3^+ to be a useful probe of the energetics of the thermosphere-ionosphere system [*Yelle and Miller*, 2004]. Specifically, H_3^+ emission is important as a major cooling agent of the Jovian thermosphere [e.g., *Miller et al.*, 1997; *Lam et al.*, 1997; *Stallard et al.*, 2002]. The major portion of all H_3^+ emission originates from the $\nu_2 = 1$ level. The study of Lam et al. showed that the auroral polar regions were emitting a few mW/m^2, with typical values of ro-vibrational temperatures ranging from 850 to 1050 K. The corresponding vertical column densities of H_3^+ were found to be 2.5 to 12.5×10^{16} m^{-2}. The relatively low spatial resolution of these measurements suggested perhaps that these cooling rates might be lower limits to actual smaller-scale auroral structures [e.g., *Grodent and Gérard*, 2001]. More recent, higher-resolution, work by *Stallard et al.* [2002] enabled auroral structures to be resolved and emission rates to be measured across the auroral/polar region. Column integrated emission rates range from 0.6 mW/m^2 (in the darkest regions) to 3.1 mW/m^2 (in the brightest regions) within the auroral oval. They also found corresponding H_3^+ column densities that varied from 0.3 to 1.4×10^{16} m^{-2}. Finally, vibrational temperatures were extracted ranging from 900 K (in the darkest regions) to 1250 K (in the brightest regions). These H_3^+ measurements provide key constraints for the present JTGCM model simulations in the auroral oval regions.

[32] Assuming that the hydrocarbon auroral emissions originate in optically thin layers, we used the simple radiative transfer model of *Drossart et al.* [1993] to calculate the effects of temperature and species abundances on the CH_4 and C_2H_2 infrared emissions. For these two molecules, the radiation is calculated for the fundamental transition which is predominant in the IR spectrum, for which optically thin conditions hold for pressures less than 20-μbar. The total emission within 2π steradians in the $\nu_4 = 1$ band of CH_4 can be written as

$$\mathbf{I_{ch4} = N_{ch4v1}\ h\ c\ E_{ch4}\ A_{ch4}/2},$$

where I_{ch4} is emission intensity, N_{ch4v1} is the integrated column of density of CH_4 in the $\nu_4 = 1$ vibrational level, E_{ch4} is the wave number (cm^{-1}) at line center (energy of the transition), and A_{ch4} is the Einstein coefficient for the vibrational transition. A similar expression can be written for C_2H_2, with the constants given in Table 1 of *Drossart et al.* [1993]. When first assuming Local Thermodynamic Equilibrium (LTE), the integrated column density $N_{ch4v1(z)}$ at level z can be calculated as given by equation (2) of

Drossart et al. The breakdown of LTE conditions for CH_4 occurs at pressures less than 1 μbars. A correction factor for non-LTE conditions is calculated which compares the quenching rate for the CH_4 molecule ($\nu_4 = 1$ levels) by H_2 and the inverse of the transition lifetime for the $\nu_4 = 1$ level. The resulting non-LTE factor reduces the total emission rate at a given level from what LTE conditions would have provided otherwise. Finally, IR cooling resulting from ethane (C_2H_6) emission is negligible in our JTGCM domain, and is therefore neglected.

[33] H_3^+ cooling in the 3–4 micron fundamental ($\nu = 2$) band is also calculated making use of the photochemically derived H_3^+ densities within the JTGCM itself. Again, it is assumed that optically thin conditions prevail. A similar cooling rate formulation is used after the hydrocarbon scheme. The quenching rate of the H_3^+ ($\nu = 2$ vibrational level) by H_2 is set at 3.0×10^{-10} cm^3sec^{-1}. The Qv(T) vibrational partition function is taken from Miller et al. (personal communication). Clearly, H_3^+ cooling is expected to maximize where local H_3^+ densities peak, in the auroral regions where production is greatest (see sections 2.5 and 2.6). This implies that H_3^+ cooling serves to offset (dampen) auroral heating as electron precipitation also provides the source for H_3^+ densities. We will later show that this H_3^+ ''thermostat'' can be important in the overall thermal balance in the Jovian upper atmosphere.

[34] The required calculated HC vertical density profiles (C_2H_2 and CH_4) were based on offline tables generated from the model of *Gladstone et al.* [1996]. Polynomial fits (up to 25th order) were constructed that reproduced zonally averaged Gladstone model HC density profiles up to 0.1 nanobars. At lower pressures (higher altitudes), HC densities are small and resulting IR cooling is minimal. The JTGCM therefore neglects HC cooling in this region.

2.5. Ion-Neutral Chemical Reactions/Rates and Production Functions

[35] A simplified set of ion-neutral chemical reactions has been collected for incorporation within the JTGCM code. Ion-neutral photochemistry is particularly important for atomic hydrogen (H) densities, since H is efficiently transported by the global circulation. Global redistribution of H modifies the local mean molecular weights, which in turn impact pressure gradients and the resulting winds. The goal of such a reduced set of chemical reactions is to capture the primary sources and sinks for atomic hydrogen, as well as H_2^+ and H_3^+. Production functions for H atoms and H_2^+ ions are utilized, based on detailed offline 1-D model calculations. The H_2^+ production function incorporates direct electron (auroral) and ion (equatorial) precipitation sources only. The production function for H is derived from net H_2 dissociation resulting from initial electron precipitation and subsequent chemical reactions (see below). Recall that the H^+ ion is presently prescribed within the JTGCM on the basis of detailed 1-D auroral profiles calculated offline [*Waite et al.*, 1983]. It is well known that a proper calculation of H^+ densities requires a loss mechanism involving H_2 vibrational levels [*Cravens*, 1987; *Majeed and McConnell*, 1991]. However, this key loss for H^+ was not properly treated within the Waite et al. 1-D model, and likewise is missing in the present JTGCM code. A future version of the JTGCM will explicitly incorporate these H_2 vibrational levels for this purpose (see section 6).

[36] Table 2 summarizes the key reactions and rates incorporated; ion-neutral reaction rates are taken from *Atreya* [1986], *Gladstone et al.* [1996], *Kim and Fox* [1994], and updated by *Moses and Bass* [2000]. Electron temperatures are assumed to be identical to neutral temperatures. Production of H_2^+ is parameterized according to the same auroral [*Waite et al.*, 1983; *Grodent and Gérard*, 2001] and equatorial [*Waite et al.*, 1997] 1-D calculations, for which consistent auroral and equatorial heating is obtained. Electron (ion) precipitation alone is considered for production of H_2^+ in the auroral (equatorial) region; this accounts for the dominant sources. Losses for H_2^+ are explicitly carried within the JTGCM code. The major (very fast) sink for H_2^+ yields H_3^+; other losses are minor. Likewise, this same strong H_2^+ sink is the dominant source of H_3^+ ions throughout the JTGCM domain. Major losses of H_3^+ are twofold: (1) dissociative recombination of H_3^+ can yield either 3H or (H + H_2), and (2) reaction with CH_4 is important at low altitudes. Dissociative recombination rates for these two branches have been the subject of considerable debate. However, the paper by *Bates et al.* [1993] and the laboratory study by *Sundstrom et al.* [1994] provide strong theoretical and experimental support for a total recombination rate of $\sim 1.5 \times 10^{-7}$ cm^3/s at 300K. According to recent measurements by *Larsson* [1997], we adopt a slightly reduced rate (1.1×10^{-7} cm^3/s at 300K) along with the branching ratios suggested by *Mitchell et al.* [1983]. The dominant ion calculated in the aurorally excited ionosphere is H_3^+, which is the predominant contributor to ion drag.

[37] The sources for atomic H are similarly prescribed on the basis of a polynomial fit to a production function calculated by the auroral 1-D model of *Waite et al.* [1983]. The H production function is constructed by assuming each H_2^+ ion created results in 2 to 4 H atoms ultimately being produced via chemical reactions culminating in H_3^+ dissociative recombination. This effective H_2 dissociation source for H can be scaled according to the initial electron precipitation source for H_2^+. This scheme enables a consistency to be maintained throughout the JTGCM for unique auroral energy inputs (see section 2.6). In addition, a weak low-latitude ion precipitation source of H is incorporated on the basis of a polynomial fit to a similar production function calculated by the equatorial 1-D code of *Waite et al.* [1997]. The major sinks of H are explicitly calculated within the JTGCM and include (1) three-body recombination (low altitude), (2) reactions with C_2H_2 and CH_4 (low altitude), and (3) charge exchange with H_2^+ (high altitude).

[38] The objective in utilizing these 1-D model production functions is to obtain detailed auroral and equatorial model inputs for the JTGCM in a cost-effective way. Both production functions for H atoms and H_2^+ ions can be scaled to allow for changing electron and ion precipitation characteristics utilized in formulating the auroral and equatorial heating rates, respectively. In this manner, internal consistency is maintained among the productions and the corresponding heating rates. Later JTGCM upgrades will provide for direct formulations of these production functions within the JTGCM itself using simplified schemes.

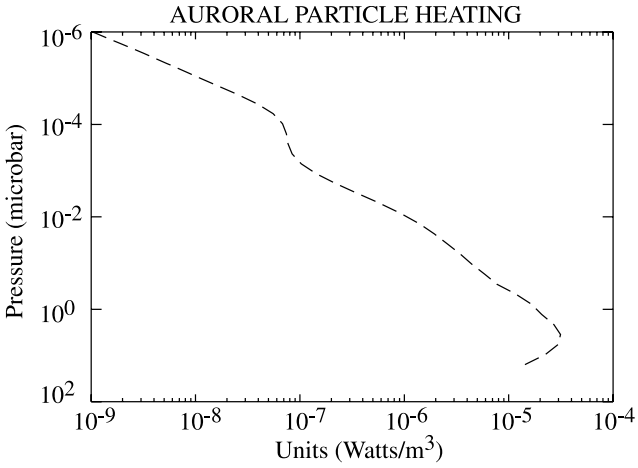

Figure 2. The vertical profile of auroral oval heating (flux ~110 mW m^{-2}) applied within the JTGCM [*Grodent and Gérard*, 2001]. This heating profile is multiplied by the auroral masking function (Figure 3), yielding λ_{III} longitudinally symmetric oval heating in the north and south. Units are W/m^3.

2.6. Auroral and Equatorial Particle Heating Parameterizations

[39] For the auroral atmosphere model used in the JTGCM, we adapt the 1-D auroral electron transport and temperature model of *Grodent and Gérard* [2001] to a three-dimensional grid. The precipitating electrons possess an energy spectrum described by a three-kappa distribution with energy distributed among three components: (1) 22 keV particles (100 mW m^{-2}), (2) 3 keV particles (10 mW m^{-2}), and (3) 100 eV particles (0.5 mW m^{-2}). The total auroral energy flux is ~110 mW m^{-2}. For each of these components, energy is roughly deposited near the homopause, just above the homopause, and high in the Jovian thermosphere, respectively [*Grodent and Gérard*, 2001]. This vertical profile for auroral oval heating due to precipitating electrons is parameterized within the JTGCM as shown in Figure 2. The major electron heating mechanisms considered in this parameterization also account for the chemical heating due to the formation of H_2^+ and H, plus subsequent reactions resulting in dissociative recombination of H_3^+ to produce H_2 and H [*Grodent and Gérard*, 2001]. It is noteworthy that the electron degradation codes used by *Grodent and Gérard* [2001] and in the JIM model [*Achilleos et al.*, 1998] produce different penetration depths for electrons of roughly the same energy. Resolution of this discrepancy is beyond the scope of this paper (see discussion in section 5).

[40] For the equatorial model atmosphere, we assume that precipitating particles may be heavy ions with energies greater than 300 keV/amu. The JTGCM uses the charged-particle "drizzle" estimated by *Waite et al.* [1997] from the ROSAT X-ray observations as a source of weak equatorial heating (flux = 0.15 mW m^{-2}). This drizzle was specified within a low-latitude band (±60° latitude) to investigate the relative importance of this heating mechanism on the Jovian equatorial thermosphere. Simulations with and without this equatorial drizzle were conducted to quantify its impact on the equatorial thermal budget. JTGCM simulations show that the heating due to this drizzle is weak compared to dynamical heating at equatorial latitudes (see section 3.2).

[41] The auroral morphology in the JTGCM code is represented by the north and south polar ovals inferred from the analysis of the Jovian ultraviolet (UV) images obtained by the HST WFPC-2 from June 1996 to July 1997 [*Clarke et al.*, 1998]. The input particle heating is specified symmetrically in λ_{III} longitude along both polar ovals, with a vertical distribution (as a function of pressure) that is the same everywhere. The oval width is limited to the 5° latitude-longitude resolution of the JTGCM code, effectively yielding a delta function for auroral forcing along the two ovals. This oval width in the JTGCM is coarser than that of Jupiter's real oval; nevertheless, the integrated energy flux is assumed to be the same. This same "mask" is applied to the auroral production functions (see section 2.5). This auroral oval "masking pattern" is illustrated in Figure 3 for the north and south ovals. Superimposed on this masking function are plotted plasma drift vectors corresponding to the magnitude and direction of the net (u_i + v_i) ion winds. Maximum arrows represent nearly 3.0 km/s ion winds in both hemispheres. Details of this single-cell ion circulation will be described in section 2.8.

2.7. Magnetic Field Model and Orientation

[42] The present state-of-the-art in Jupiter magnetic field mapping is described in detail by *Connerney et al.* [1998], who discussed the origins and limitations of the two primary magnetic field models presently in use. The VIP4 model has been improved over the O6 model by the use of HST and IRTF images of the latitude track of the Io flux tube. This guarantees a better agreement in the field line mapping to the region of the Io orbit. However, it may not improve the fits for more distant regions (near the 30–50 Rj limit of the field model). The VIP4 magnetic field model is used within

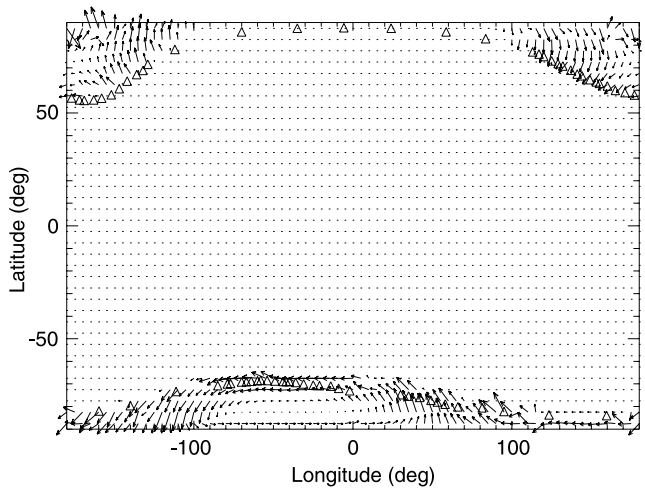

Figure 3. The auroral masking function (open triangles) yielding λ_{III} longitudinally symmetric oval heating and production functions in the north and south. Taken from HST observations of *Clarke et al.* [1998]. Superimposed ion drift vectors are also added, revealing single cell circulation patterns in the north and south oval regions. Maximum vectors correspond to plasma drifts up to ~3.0 km/s.

the JTGCM formulations to (1) specify the ion drag parameters and (2) map the Jovian magnetosphere to the ionosphere.

2.8. Ion-Drag and Joule Heating Formulations

[43] Ion-drag, which modifies neutral wind speeds in the Jovian thermosphere, is produced by ion-neutral collisions in the Jovian auroral oval regions. Ions, magnetically connected to the subrotating regions of the magnetosphere, lose their momentum in collisions with neutrals and thus drive the neutrals to move in roughly the same direction. This drag is proportional to the product of the ion density (mostly H_3^+) and the relative drift between the neutral and ion constituents. Ion-drag is a dominant neutral momentum forcing process at auroral oval latitudes near the altitude of the ionospheric peak. In addition, Jovian high latitudes map furthest into the Jovian magnetosphere, along magnetic field lines ($L \geq 20$); the corresponding ions are subject to corotation breakdown and thereby influence the corotating neutrals in unique ways. Ion drag also depends on the ion-neutral collision frequency and on the local configuration of the magnetic field. At higher ionospheric altitudes where the ion gyrofrequency exceeds the ion-neutral collision frequency, ionization is constrained to move along field lines, thereby dragging the neutrals. In addition, Joule heating results from the friction due to the motion of the ions relative to the neutrals. *Richmond et al.* [1992] have shown that ion-drag can significantly modify the neutral winds at Earth's low and mid latitudes, thereby affecting the distribution of neutral temperatures.

[44] The parameterization of ion-drag and Joule heating in the JTGCM code is based on the formulation described by *Roble and Ridley* [1987]. The ion-drag parameters (tensors) for the 10° offset Jovigraphic and Jovimagnetic poles are described as follows:

$$\lambda_{xx} = \lambda_1\left(\mathbf{1} - \mathbf{sin}^2\delta\ \mathbf{cos}^2\mathbf{I}\right),$$

$$\lambda_{yy} = \lambda_1\left(\mathbf{1} - \mathbf{cos}^2\delta\ \mathbf{cos}^2\mathbf{I}\right),$$

$$\lambda_{xy} = \lambda_1\mathbf{sin}\delta\mathbf{cos}\delta\ \mathbf{cos}^2\mathbf{I} + \lambda_2\mathbf{sinI},$$

$$\lambda_{yx} = \lambda_1\mathbf{sin}\delta\mathbf{cos}\delta\mathbf{cos}^2\mathbf{I} + \lambda_2\mathbf{sinI},$$

where δ is the magnetic declination angle and I is the magnetic dip angle and

$$\lambda_1 = \sigma_P\mathbf{B}^2/\rho,$$

$$\lambda_2 = \sigma_H\mathbf{B}^2/\rho,$$

where σ_P and σ_H are the Pedersen and Hall electrical conductivity, respectively, B is the strength of the magnetic field from the VIP4 model of *Connerney et al.* [1998], and ρ is the JTGCM density. The Joule heating (per unit density) in the JTGCM is derived from the ion-drag parameters as

$$\mathbf{Q}_J = \lambda_{xx}(\mathbf{u}_i - \mathbf{u}_n)^2 + \lambda_{yy}(\mathbf{v}_i - \mathbf{v}_n)^2 + \left(\lambda_{xy} - \lambda_{yx}\right)(\mathbf{u}_i - \mathbf{u}_n)(\mathbf{v}_i - \mathbf{v}_n),$$

where u_i and v_i are the Jovigraphic zonal and meridional ion drift velocities; u_n and v_n are the zonal and meridional neutral wind components determined at a given time step in the JTGCM. A convection electric field is estimated and corresponding ion drifts (u_i and v_i) are generated using an ionospheric convection model based on Voyager measurements of ion convection in the outer magnetosphere [cf. *Eviatar and Barbosa*, 1984]. Subsequently, the VIP4 magnetic field model [*Connerney et al.*, 1998] is used to map this magnetospheric ion convection pattern to ionospheric altitudes at auroral oval latitudes. In this manner, anticorotational electrojet winds of nearly 3.0 km/s are prescribed around both main auroral ovals, driving the neutral winds to move in the same direction. Conversely, in nonauroral regions, u_i and v_i are zero (i.e., corotational); corresponding neutral winds are decelerated by ion-drag forcing in those regions where the ion-neutral collision frequency remains high.

[45] These well-tested TIGCM formulations provide a means to examine the general impact of ion drag and Joule heating on the JTGCM neutral winds and thermospheric structure. A future JTGCM paper will examine in great detail the coupling of the Jovian ionosphere and magnetosphere, and the time variable nature of this magnetospheric ion convection pattern and its ionospheric counterpart.

3. JTGCM Simulations and Results

[46] Three simulations from the JTGCM are examined in detail in this section: (1) a simplified case incorporating moderate auroral forcing (particle precipitation) alone; (2) a coupled case combining auroral plus reduced (30%) ion drag and corresponding moderate Joule heating; and (3) a coupled case incorporating auroral, full (100% efficient) ion drag, plus strong Joule heating. The goal in selection of these three cases (see Figure 1) for detailed study is to provide representative simulations of Jupiter's upper atmosphere for which the relative roles of the underlying dynamical drivers can be clearly identified and investigated. The evolution of these three cases toward a best simulation, reasonably matching available multispectral and Galileo probe measurements, seems the best suited to this goal. In addition, a great deal of computer time is required to achieve steady-state conditions for each of these simulations utilizing the required 60 second time step. We identify common slices of JTGCM output fields to present for each case to facilitate model comparisons. Specifically, fields at constant pressure levels (near the model top and H_3^+ peak), zonal average fields over the entire JTGCM domain, and an assortment of energy diagnostic terms are illustrated and described for each case. The model near-top level is located at $\sim 2.0 \times 10^{-4}$ nbar; the H_3^+ peak is typically located at $\sim$0.14-μbar.

3.1. Moderate Auroral Forcing Alone

[47] Case 1 is initiated with auroral forcing alone; ion drag and Joule heating are neglected. This case is run to steady state for 40-Jovian rotations. This simplified simulation affords us the opportunity to examine the strength of the global wind system and its ability to transport energy and species about the planet for moderate auroral forcing conditions without the complexity of thermosphere/iono-

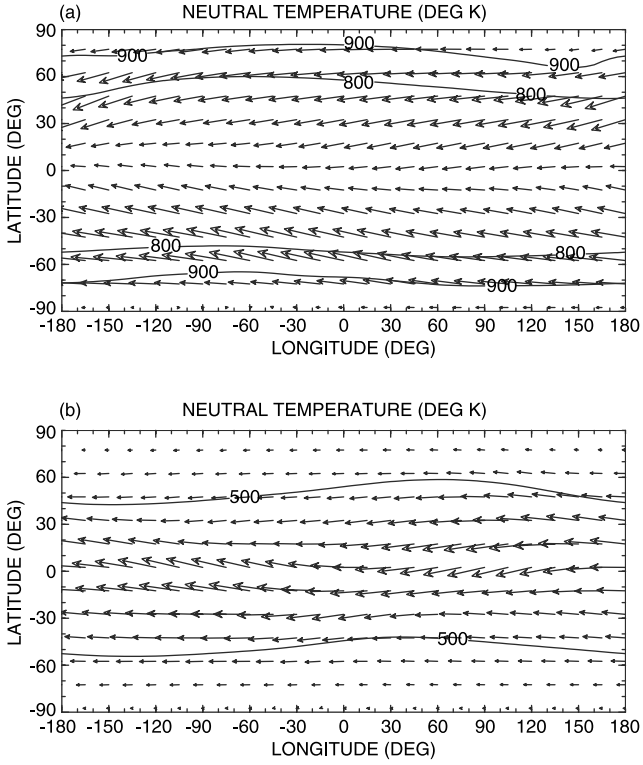

Figure 4. JTGCM Case 1 (auroral forcing alone). Superimposed neutral temperature (T) plus wind vectors (U + V) indicating the magnitude and direction of the horizontal winds. Pressure level slices at the (a) model top (1.1×10^{-4} nbar) and (b) H_3^+ peak level (0.14-μbar) are given. These levels correspond roughly to 2400 and 400 km, respectively. Temperature intervals are 100K, ranging from (a) 800 to 900 K and (b) 400 to 500 K. Maximum horizontal winds range from (a) 550 to (b) 180 m/s. Wind vector lengths are independently scaled to the maximum vector wind speeds for Figures 4a and 4b.

sphere/magnetosphere coupling. Cases 2 and 3 will incorporate these coupling processes for different efficiencies (see sections 3.2 and 3.3).

[48] Figure 4a shows JTGCM aurorally driven temperature and horizontal wind distributions near the top boundary of the JTGCM in the exosphere. These neutral winds clearly diverge from the auroral oval regions (in the north and south), are rapidly turned westward by the strong Coriolis forces, and converge at low latitudes. Corresponding temperatures are warmest in the oval regions themselves (reaching ~950 K), and much cooler at lower latitudes and near the equator (~700 K). These exospheric temperatures are roughly 250 K colder than observed in the auroral oval regions [e.g., *Drossart et al.*, 1989; *Miller et al.*, 1990; *Lam et al.*, 1997] and near the equator [cf. *Seiff et al.*, 1998]. Some modest component of the meridional winds is visible in the upper thermosphere, yielding a net maximum horizontal (zonal plus meridional) wind of approximately 500 m/s. Corresponding exospheric vertical winds are upward (+1.0 to 7.0 m/s) in the oval regions in accord with divergent flow, and downward (−0.5 to −1.0 m/s) at low latitudes where the global thermospheric flow converges. Conversely, Figure 4b illustrates aurorally driven temperature and horizontal wind distributions near the H_3^+ peak. Clearly, zonal winds dominate (up to 150 m/s), meridional and vertical winds are very weak, and divergence and convergence of this flow is hard to identify. At this level (p = ~0.14-μbar), the net thermal forcing and resulting meridional flow are not sufficient to overcome the strong Coriolis forces. Further details on momentum balances will be given below in the context of zonal average quantities.

[49] Zonal average slices for several JTGCM fields are presented over 6 panels in Figure 5. These slices provide insight into the longitude independent wind, temperature and density distributions for comparison to available multispectral data. The largest latitudinal temperature gradients (up to 250 K) are found above 700 km (below 0.01 μbar) (Figure 5a). The resulting zonal (Figure 5b) and meridional (Figure 5c) winds are largest above 700 km as well. Zonal jets with westward winds up to ~450 m/s appear at 40–60° latitude in both hemispheres; corresponding meridional flow is equatorward in both hemispheres with magnitudes reaching 140 m/s. Below ~700 km, meridional flow is very weak and the zonal jet structure breaks down. Resulting vertical winds (Figure 5d) are upward in both polar regions (approaching 4.0 m/s) and downward near the equator (up to −1.0 m/s), again reflecting the fact that the strongest global wind structure (largely symmetric between the hemispheres) occurs above 700 km.

[50] A quantitative measure of the relative importance of the Coriolis torques requires that momentum balances be examined as a function of altitude for this Case 1 simulation. For zonal averaged conditions (not shown), a comparison of meridional momentum terms above 1300 km reveals that pressure gradient terms driving meridional winds are larger than Coriolis terms, with molecular viscosity becoming important at the highest altitudes. A similar comparison of terms below 1300 km demonstrates that Coriolis torques are largely balanced by meridional pressure gradients, consistent with geostrophic balance. Hence the threshold magnitude of zonal averaged meridional winds required to overcome Coriolis forces is approximately ~100 m/s. This threshold is achieved in the upper thermosphere, but not near the 0.14-μbar level for this JTGCM Case 1 simulation.

[51] Compositional distributions respond both to the large scale circulation and the background temperature structure. Figure 5e presents the zonal average atomic hydrogen distribution, showing an aurorally driven peak ($\sim 6.1 \times 10^{10}$ cm^{-3}) near 1.5-μbar in both hemispheres. Below ~600 km, the pole-to-equator decrease in the hydrogen density on a constant pressure surface reflects cooler equatorial temperatures. However above ~700 km, the hydrogen densities transition to a more uniform latitudinal distribution owing to meridional transport which is beginning to be effective. Overall, the latitudinal density variation is quite weak, implying that hydrogen is largely controlled by photochemical sources and sinks, the local temperature distribution, and vertical diffusion. Equatorward transport of hydrogen only begins to be important above 700 km, resulting in the lateral redistribution of hydrogen atoms. Finally, Figure 5f illustrates the H_3^+ (primary ion) latitudinal distribution, for which a peak ($\sim 1.5 \times 10^5$ cm^{-3}) is observed in the southern oval region near 0.14-μbar, and low-latitude (±50°) values maximize near the same pressure level reaching $\sim 5-8 \times 10^4$ cm^{-3}. See also Figures 6a

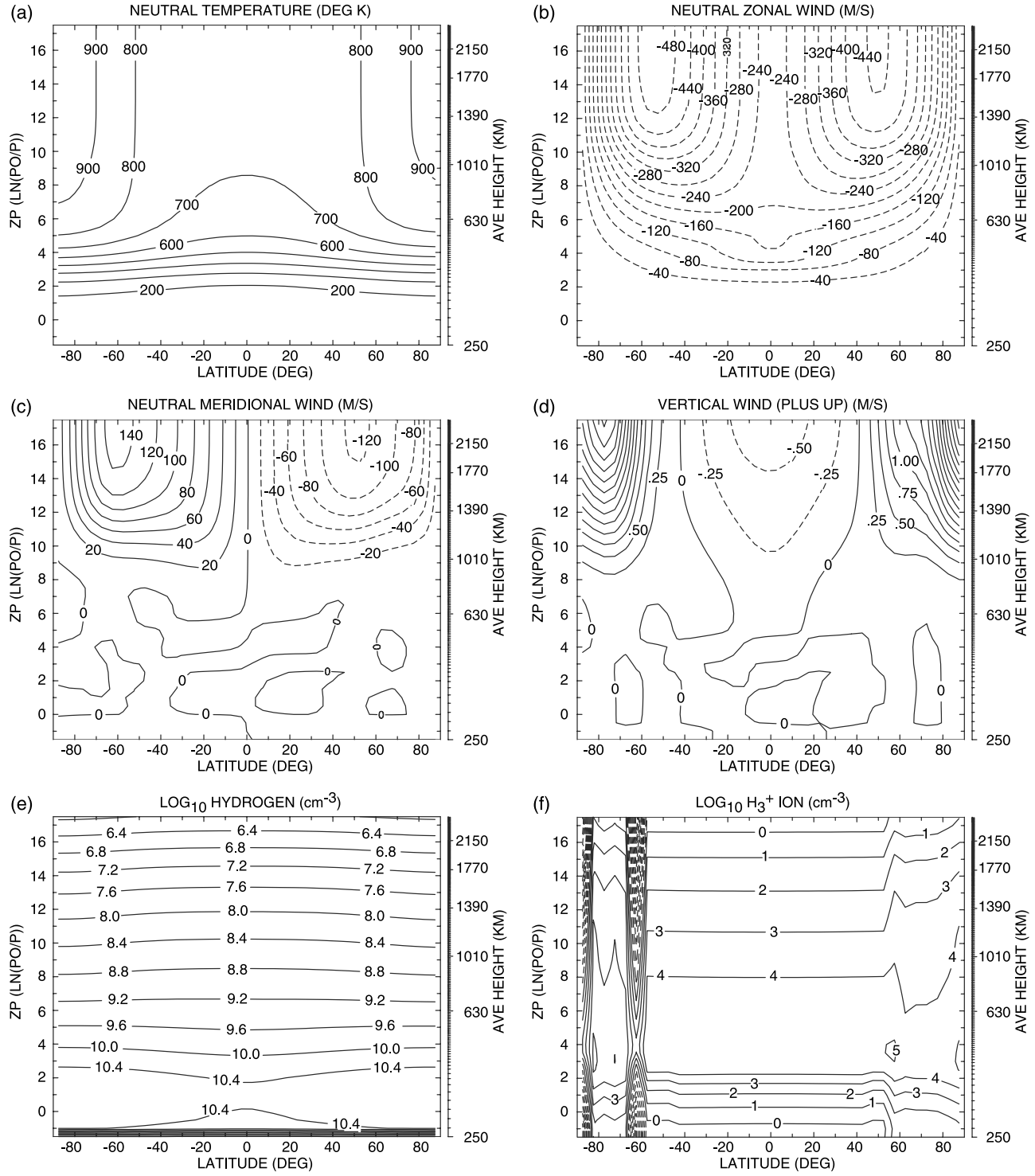

Figure 5. JTGCM Case 1 (auroral forcing alone). Zonal average slices over the entire JTGCM vertical domain (in log pressure coordinates with a corresponding average height axis). The reference pressure level (p0) is 4.5 μbar. Fields include (a) temperature (T) in 100 K intervals; (b) neutral zonal winds (U) in 40 m/s intervals; (c) neutral meridional winds (V) in 20 m/s intervals; (d) neutral vertical winds (W) in 0.25 m/s intervals; (e) atomic hydrogen (H) in 0.4 intervals of $\log_{10}$ units (#/cm^3); and (f) H_3^+ density in 1.0 intervals of $\log_{10}$ units (#/cm^3). Dashed lines indicate negative winds: zonal (westward), meridional (southward), and vertical (downward). Figure 5e and 5f densities ($\log_{10}$ #/cm^3) can be converted to $\log_{10}$ #/m^3 units by adding 6.0 to the contour intervals.

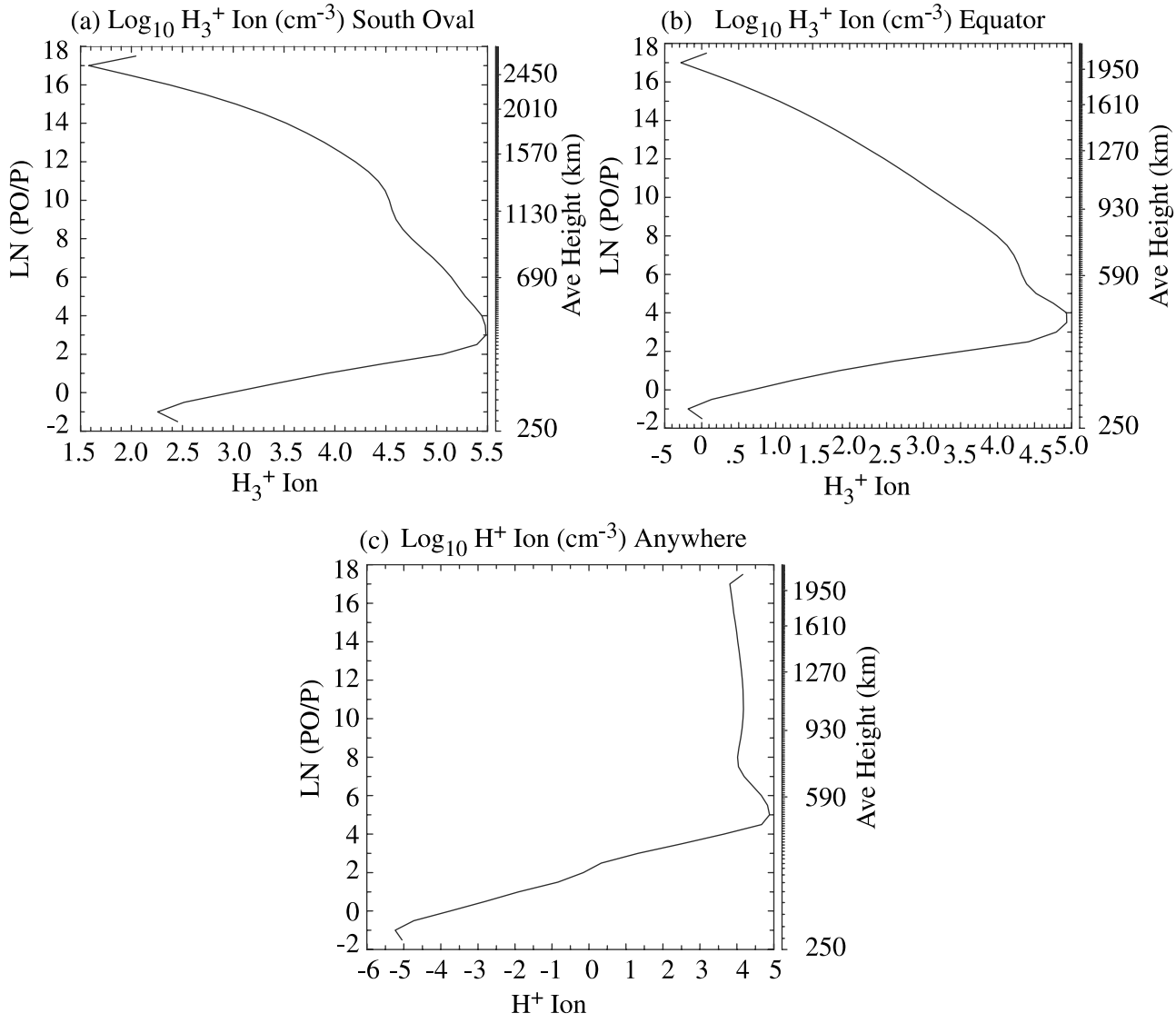

Figure 6. JTGCM Case 1 (auroral forcing alone). Ion density profiles are contrasted for auroral versus equatorial regions. Specifically, (a) a typical H_3^+ density profile within the south oval (aurorally driven), (b) an H_3^+ density profile at the equator (including drizzle), and (c) an H^+ density profile anywhere (prescribed from an independent 1-D model). Units are $\log_{10}$ #/cm^3 for each panel, for ease of comparison with Figure 5f. These densities can be converted to $\log_{10}$ #/m^3 units by adding 6.0 to the profile values.

and 6b. The northern oval region is sufficiently smeared out in a zonal average plot so that discernable ion peaks are not as clearly visible as those in the south.

[52] Compositional distributions can also be presented in mixing ratio units, thereby eliminating the effects of temperature changes (i.e., thermal expansion) and highlighting the influence of chemistry and transport effects of the global circulation. However, the zonal average distribution (not shown) of the atomic hydrogen mixing ratio (H/H_2) reveals only a weak variation from pole-to-equator above ~700 km. Below, a ~1.0% enhancement of this ratio occurs from the equator to the auroral oval regions. This behavior is not controlled by lower boundary conditions (nearly 2 scale heights away). Rather, this variation is consistent with (1) high-latitude sources of atomic H dominating near this level and (2) the transport of hydrogen atoms becoming effective above ~700 km.

[53] Ion distributions within the southern oval (H_3^+) and near the equator (H_3^+ and H^+) are also presented in Figure 6 to clearly identify where the major ion peaks are located and their magnitude for this moderate auroral case. Figure 6a shows the H_3^+ ion peaking near 0.14-μbar (about 550 km) at ~3.0×10^5 cm^{-3} in the southern oval region. The auroral source for the H_3^+ ion is provided by electron precipitation, as parameterized by the H_2^+ production function utilized by the JTGCM (see section 2.6). Nonoval production of H_3^+, owing to charged particle (ion) drizzle from the inner radiation belts, gives rise to an equatorial peak near 0.14-μbar of ~8.6×10^4 cm^{-3} (Figure 6b). Finally, the H^+ profile is prescribed uniformly about the

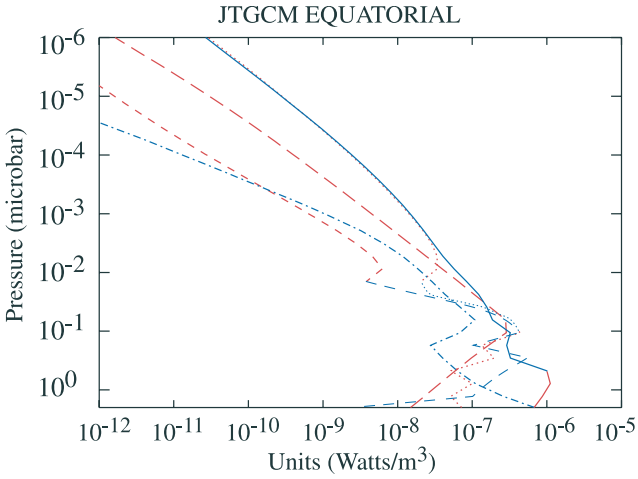

Figure 7. JTGCM Case 1 (auroral forcing alone). Heat balance plot at the equator comparing various terms as a function of pressure (units of W/m^3). IR cooling is derived from both hydrocarbon and H_3^+ (2–4 micron) emission. Red curve segments denote heating; blue curve segments denote cooling. Individual curves are delineated as follows: (1) conduction (solid), (2) adiabatic heating/cooling (dotted), (3) IR cooling (dot-dashed), (4) drizzle heating (long dashed), and (5) hydrodynamic advection (short-dashed).

planet, as illustrated in Figure 6c. The peak density of $\sim 1.0 \times 10^5$ cm^{-3} is found near 0.03-μbar. Topside H^+ densities are somewhat high, consistent with the fact that vibrationally excited H_2 is not included in the *Waite et al.* [1983] 1-D model, nor in the present JTGCM prescription (see section 2.5). Overall, the major ions (H_3^+ and H^+) have slightly separated peak heights, with H_3^+ ions peaking at the lowest altitudes.

[54] Diagnostics are obtained to confirm those processes that maintain the equatorial and auroral region simulated temperatures for Case 1. Auroral thermal balances (not shown) reveal that the prescribed auroral heating (Figure 2) is largely offset by molecular thermal conduction and to a lesser extent upwelling winds (adiabatic cooling) in the upper thermosphere. This downward conducted heat is subsequently radiated away by H_3^+ emission (hydrocarbon emission) above (below) the CH_4 homopause near 4.5-μbar. Overall, dynamical terms have little influence on auroral thermal balances in this JTGCM simulation; i.e., radiative equilibrium largely prevails. Conversely, equatorial thermal balances (Figure 7) reveal that adiabatic heating plus weak charged-particle drizzle combine to maintain temperatures above ~350 km (at pressures below 0.1 μbar). Figures 5c and 5d confirm that winds subside and converge near the equator providing modest dynamical heating. Heating and cooling rates at 0.1-μbar approach 2×10^{-7} Wm^{-3}. Molecular thermal conduction acts to direct this heat downward toward the CH_4 homopause where hydrocarbon IR cooling radiates the heat away. Just above the homopause (0.1 to 1.0 μbar), adiabatic heating and horizontal advection terms also contribute to this downward conducted heat, giving rise to the strong vertical temperature gradient calculated. However, the simulated heating terms are not sufficient to maintain the observed equatorial temperatures of the Galileo ASI profile [*Seiff et al.*, 1998]. Another source of equatorial heating is required to reproduce Galileo ASI temperatures.

[55] In summary, this aurorally driven JTGCM simulation illustrates the response of the equatorial thermospheric temperatures and hydrogen densities to modest equatorward neutral winds at high altitudes. However, below 700 km, the auroral forcing is not strong enough to drive meridional winds that can impact the thermospheric structure near the equator. Measured Galileo ASI temperatures are impossible to reproduce with this wind structure. A threshold level of equatorward wind magnitudes is required to overcome the strong Coriolis forces in the Jovian upper atmosphere. This Case 1 JTGCM simulation suggests that meridional wind speeds must exceed roughly 100 m/s for equatorial densities and temperatures to be noticeably affected by high-latitude forcing.

3.2. Moderate Auroral Forcing Plus Reduced Ion Drag and Joule Heating

[56] Case 2 incorporates both auroral forcing plus ion drag. The latter is prescribed according to a plasma drift pattern (Figures 3 and 8) that is consistent with a convection electric field derived from the Voyager constrained magnetosphere model of *Eviatar and Barbosa* [1984] (see section 2.8). For this JTGCM case, reduced (30%) ion drag and corresponding moderate Joule heating are incorporated into the JTGCM. This ion drag efficiency means that a 30% scaling of the full ~3.0 km/s maximum ion winds is implemented in the JTGCM. Such a scaling may correspond to a smaller convection electric field than estimated from the Eviatar and Barbosa model. Case 3 will incorporate the full ion winds for calculation of ion drag and corresponding strong Joule heating. Both Case 2 and 3 simulations are run for 55–65 Jovian rotations in order to ensure that steady state solutions are achieved below ~1.0 μbar.

[57] Figure 8 illustrates the underlying single-cell plasma drift patterns (north and south) that give rise to the ion drag forcing newly implemented in the Case 2 JTGCM simulation. These polar plots show that anticorotational ion flow expected for an auroral electrojet prevails in both the southern and northern hemispheres. The length of the arrows signifies relative ion wind speeds at the JTGCM grid points corresponding to the prescribed oval locations. The ion wind patterns are pronounced and well organized in both hemispheres; the northern hemisphere circulation cell extends over a wider range of Jovigraphic latitudes (57–90°N) than in the southern hemisphere (65–90°S). In both cells, zonal ion winds approach ~3 km/s, while meridional ion winds are weaker (up to 1.5 km/s). In general, the southern hemisphere plasma drifts are slightly (20%) stronger than those in the north, owing to the mapping of VIP4 magnetic field lines further outward into the Jovian magnetosphere. Such mapping results in a larger departure of the southern hemisphere plasma drifts from corotation than plasma drifts in the north.

[58] Figure 9a shows the JTGCM Case 2 temperature and horizontal wind distributions near the top boundary of the JTGCM in the exosphere; direct comparisons can be made with Figure 4a. Neutral thermospheric winds still diverge from the auroral oval regions (in the north and south), with maximum vector neutral winds now reaching ~1.2 km/s.

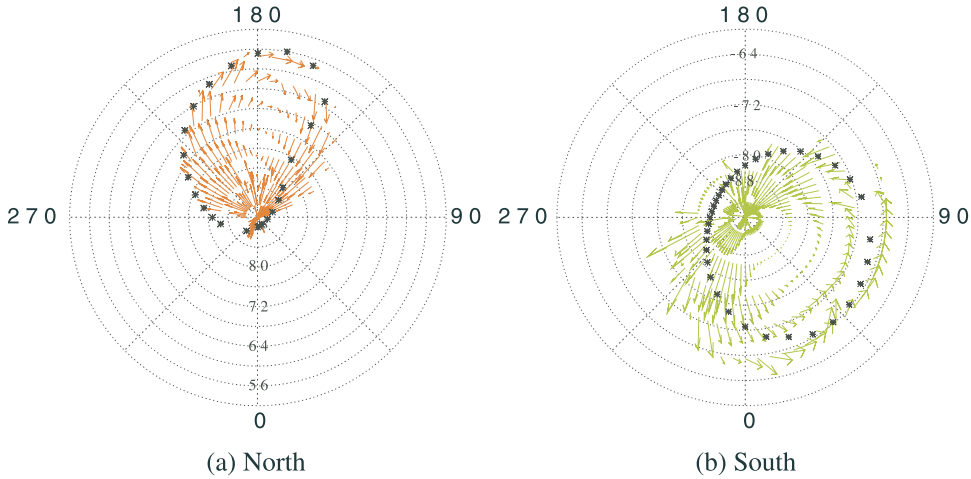

(a) North (b) South

Figure 8. JTGCM Case 2 (auroral forcing plus scaled ion drag). Plasma drift flow vectors (u_i and v_i) plotted on polar dials in the (a) north and (b) south. Vectors represent the magnitude and direction of the net horizontal ion winds. Latitude circles on these dials are spaced in 4° intervals ranging from 52°N to 88°N (north oval) and 60°S to 88°S (south oval). Notice a single cell anticorotational plasma flow pattern in each hemisphere, i.e., clockwise (northern oval) and counterclockwise (southern oval). The strongest vector ion wind arrows roughly coincide with the prescribed oval locations (as indicated by the asterisks). This is in accord with the expected auroral electrojet in each hemisphere. Maximum zonal ion (u_i) winds approach ~3.0 km/s; corresponding meridional (v_i) winds approach ~1.5 km/s.

These horizontal wind speeds are more than double those presented in Case 1 (Figure 4a). Maximum exospheric temperatures now range from 1500–1600 K in both auroral oval regions to ~1350 K near the equator. These exospheric temperatures are ~600 K warmer than corresponding Case 1 values (Figure 4a). It is important to recognize that this top level within the JTGCM (near $\sim 2.0 \times 10^{-4}$ nbar) is far removed from any Jovian measurement of thermospheric temperatures [e.g., *Waite and Lummerzheim*, 2002].

[59] Instead, Figure 9b illustrates JTGCM Case 2 temperature and horizontal wind distributions near the H_3^+ peak (~0.14-μbar) which occurs in the vicinity of 500–600 km. At this level, temperatures now range from 1100–1300 K in both auroral oval regions to ~950 K near the equator; these values match available multispectral observations and Galileo ASI values reasonably well [e.g., *Lam et al.*, 1997; *Seiff et al.*, 1998; *Waite and Lummerzheim*, 2002]. In Figure 9b, a distinct single-cell pattern of strong neutral winds occurs between 60 and 90° Latitude in both hemispheres. In the southern oval region, a counterclockwise wind pattern emerges, with net vector winds reaching nearly 1.2 km/s. Zonal winds (not shown) display a very strong westward jet (up to −0.95 km/s) at high southern latitudes, with a return flow (up to +0.7 km/s) closer to the pole. The corresponding meridional winds are equatorward (up to ~0.9 km/s) and poleward (up to −0.9 km/s). The net result is a single-cell (anticorotational) neutral wind pattern that is driven by the prescribed ion winds (with 30% efficiency) illustrated in Figure 8. Similarly in the northern oval region, a clockwise single-cell (anticorotational) neutral wind pattern is visible that responds closely to the electrojet in the northern hemisphere. However, the neutral wind speeds in the northern oval region are about 50–60% of the corresponding values of the southern hemisphere.

[60] Why are the southern hemisphere (oval region) neutral winds stronger than their counterpart in the north? Ion drag is more effective in the southern auroral oval region, in part due to the ~20% larger maximum vector ion winds which are mapped from the magnetosphere to the ionosphere (see Figure 8). In addition, the local topology of the VIP4 magnetic field in the northern hemisphere is much different from that in the south [cf. *Connerney et al.*, 1998]. For the same electron densities, calculated Pedersen conductivities are generally larger in the southern hemisphere compared to those in the northern hemisphere. JTGCM diagnostics reveal a 30–40% larger column integrated Pedersen conductivity in the southern oval region (up to 20 mhos) compared to that in the north (up to 12.5 mhos). Finally, a geometric effect occurs for which the spatially larger southern hemisphere drift pattern gives rise to ion drag forcing (and Joule heating) that is continuously applied to the southern auroral oval region over a larger fraction of a Jovian day. Overall, these features determine that the enhanced ion drag and the associated stronger Joule heating combine to drive stronger neutral winds in the southern auroral oval region. In general, it is clear that the ion drag and Joule heating inputs have significantly modified the neutral wind patterns and temperature distributions in both the northern and southern auroral oval regions.

[61] Zonal average slices of Case 2 temperature, wind, and composition fields are presented (see Figure 10) for comparison to similar slices from Case 1 (Figure 5). Again, this zonal average view emphasizes latitudinal variations and affords us the opportunity to more easily compare different JTGCM simulations. Immediately, it is evident that Case 2 temperatures throughout the thermosphere are much warmer (Figure 10a) than Case 1 values (Figure 5a). Joule heating significantly modifies the heat budgets in both hemispheres, yielding warm exospheric temperatures of 1400–1600 K in both auroral oval regions. Temperatures in the vicinity of 500–600 km, near the H_3+ ion peak, are calculated to be 950 K (equatorial) to 1200–1300 K (polar).

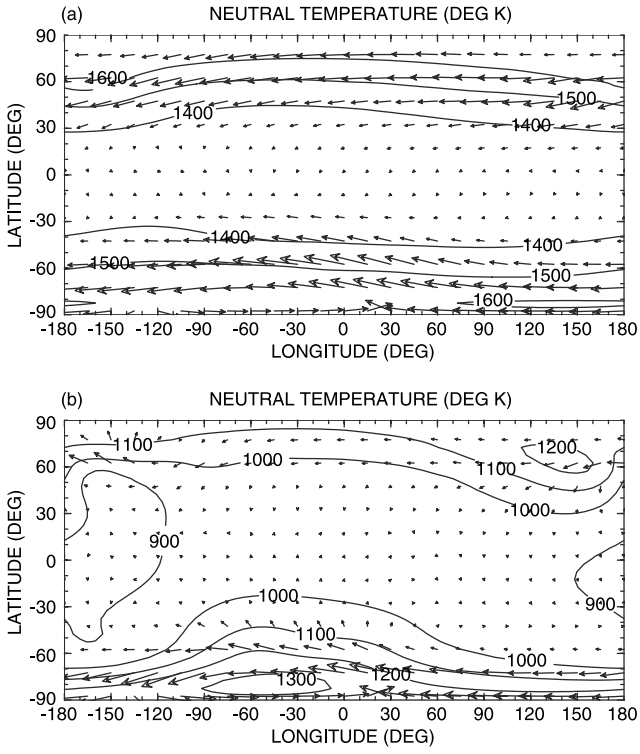

Figure 9. JTGCM Case 2 (auroral forcing plus scaled ion drag). Superimposed temperature (T) plus wind vectors (U + V) indicating the magnitude and direction of the horizontal winds. Pressure level slices at the (a) model top (1.1×10^{-4} nbar) and (b) H_3^+ peak level (0.14-μbar) are given. These levels correspond roughly to 3600 and 500 km, respectively. Temperature intervals are 100K, ranging from (a) 1400 to 1600 K and (b) 900 to 1300 K. Maximum horizontal winds range from (a) 1.15 to (b) 1.2 km/s. Wind vector lengths are independently scaled to the maximum vector wind speed for Figures 9a and 9b.

These latter values are in general accord with auroral temperatures derived from observations of H_3+ emissions [e.g., *Drossart et al.*, 1989; *Miller et al.*, 1990; *Lam et al.*, 1997] and equatorial temperatures taken from the Galileo ASI entry profile [cf. *Seiff et al.*, 1998]. Notice the strongest vertical temperature gradient appears near the equator over 1.0 to 0.05-μbar (∼400–700 km); this region overlaps the strong temperature gradient observed in the Galileo ASI profile. The heating mechanism responsible within this JTGCM simulation is examined below and in section 4. The warm topside temperatures yield large H_2 scale heights and a greatly expanded height scale as indicated on the y axis of all Figure 10 plots.

[62] The meridional temperature gradients aloft (above ∼1200 km) approach 200–300 K; latitudinal temperature gradients below 800 km are even larger near the southern oval region (60–90°S). These large gradients in the southern hemisphere give rise to a deep zonal jet centered at 70°S latitude, with winds speeds reaching −0.93 km/s (see Figure 10b). This westward jet clearly dominates the zonal flow, extends throughout most of the Jovian thermosphere (above the CH_4 homopause), and is consistent with strong meridional (south to north) winds approaching 140 m/s (see Figure 10c). Just above the homopause at high southern latitudes, the westward zonal flow weakens dramatically, and is replaced by strong poleward (Figure 10c) and subsiding (Figure 10d) flow which yields considerable dynamical heating at pressures above ∼1.0-μbar. This dynamical heating is driven by the unique neutral circulation that results directly from ion drag forcing poleward of the southern auroral oval. Further discussion of the impact of this dynamical heating is given in section 4.

[63] In the northern hemisphere, the westward zonal jet is centered at 60°N latitude, with winds speeds rising to −0.75 km/s (see Figure 10b); associated equatorward winds peak at −170 m/s (see Figure 10c). Corresponding vertical winds are strongly upward in the southern hemisphere (up to +3.5 m/s), downward at low latitudes (0.5–1.0 m/s), and upward again near the north pole (up to +6.5 m/s) (see Figure 10d). Clearly, a strong zonally averaged circulation results from the added Joule heating, with upwelling/divergent winds at both poles, and convergent/downwelling flow near the equator. Maximum neutral horizontal winds (up to 1.2 km/s) are nearly double those simulated without Joule heating in Case 1. The slight hemispheric asymmetry in the calculated zonal averaged winds reflects the underlying asymmetries in the ion drag and Joule heating terms described above.

[64] This strong interhemispheric circulation pattern is clearly reflected in the hydrogen distribution (Figure 10e), for which pole to equator density gradients (above 1200 km) can be as large as a factor of 200 or more. Hydrogen atoms created largely in the polar regions are being efficiently transported equatorward following zonally averaged streamlines of the global circulation pattern. This process of "wind induced diffusion" favors species with scale heights that are large compared to the background mean atmosphere. Therefore the hydrogen distribution is a good tracer of the Jovian thermospheric circulation. Lyman-α emission maps can be compared with JTGCM model predictions making use of the calculated hydrogen distribution in order to constrain the global thermospheric circulation pattern during observational periods (see further discussion in section 4). Finally, Figure 10f illustrates the H_3^+ ion distribution, for which a peak ($\sim 2.0 \times 10^5$ cm^{-3}) is observed in the southern oval region near 0.14-μbar, and low-latitude (±50°) values maximize near the same pressure level and slightly smaller magnitude. These H_3^+ ion densities are somewhat larger than for Case 1, which is consistent with warmer neutral (and electron) temperatures and less efficient dissociative recombination (primary loss) of H_3^+ (see section 2.5).

[65] Pedersen conductivities are calculated in both the southern and northern oval regions and plotted in Figures 11a (south oval) and 11b (north oval) in order to demonstrate that hemispheric differences exist. Conductivity profiles are chosen for display that appear near the local maxima of the VIP4 magnetic field map, i.e., south oval (72.5°S latitude; 0° λ_{III} longitude) and north oval (57.5°N latitude; 180° λ_{III} longitude). Peak values appear in the vicinity of the local H_3^+ ion peak; values are 3.176×10^{-4} mhos m^{-1} (south oval) and 2.350×10^{-4} mhos m^{-1} (north oval). These specific profiles illustrate the role that the local VIP4 topology has on the simulated Pedersen conductivities. A maximum 35% difference between the

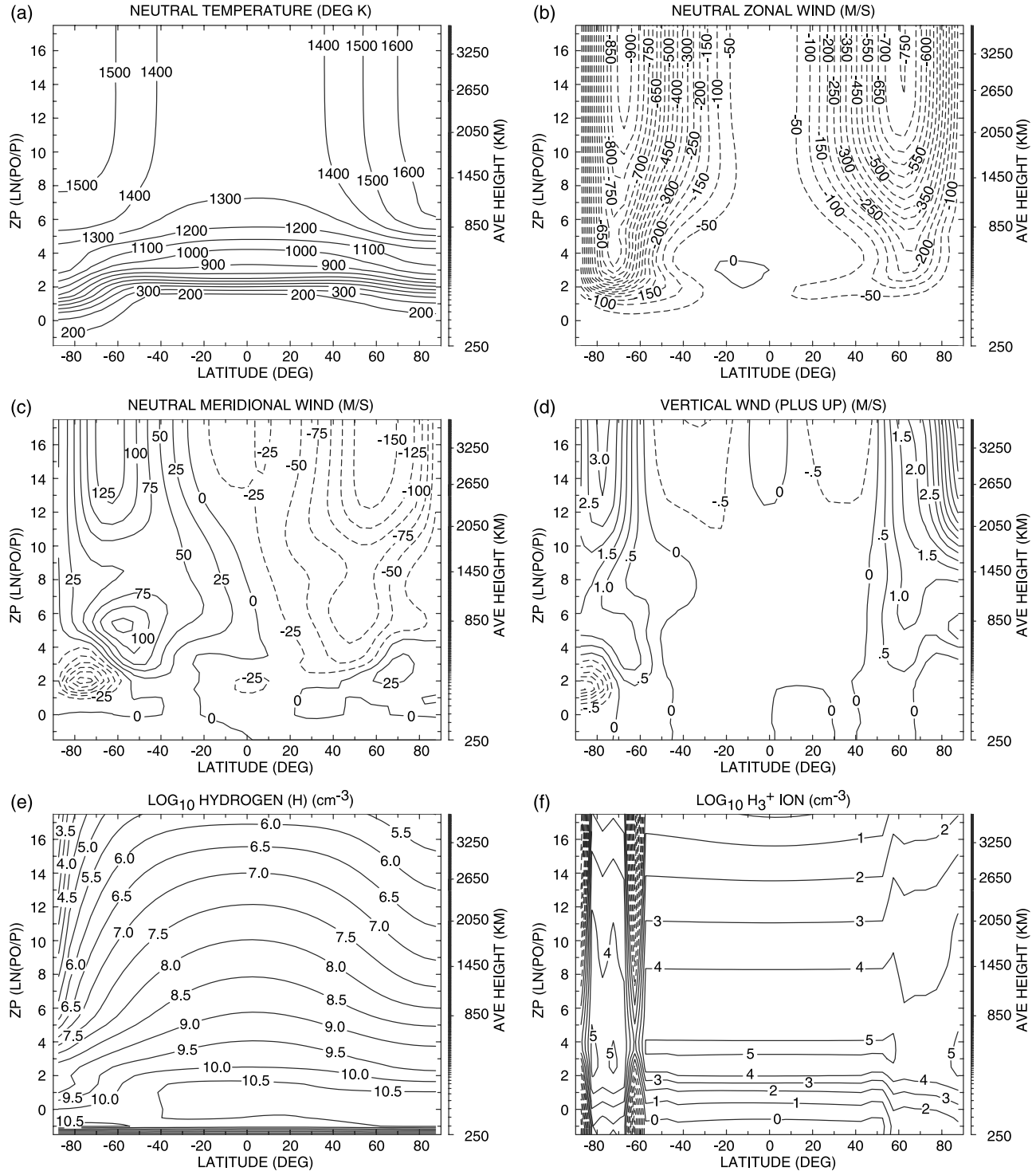

Figure 10. JTGCM Case 2 (auroral forcing plus scaled ion drag). Zonal average slices over the entire JTGCM vertical domain (in log pressure coordinates). Fields include (a) temperature (T) in 100 K intervals; (b) neutral zonal winds (U) in 50 m/s intervals; (c) neutral meridional winds (V) in 25 m/s intervals; (d) neutral vertical winds (W) in 0.5 m/s intervals. (e) atomic hydrogen (H) in 0.5 intervals of $\log_{10}$ units (#/cm^3); and (f) H_3^+ density in 1.0 intervals of $\log_{10}$ units (#/cm^3). Dashed lines indicate negative winds: zonal (westward), meridional (southward), and vertical (downward). Figure 10e and 10f densities ($\log_{10}$ #/cm^3) can be converted to $\log_{10}$ #/m^3 units by adding 6.0 to the contour intervals.

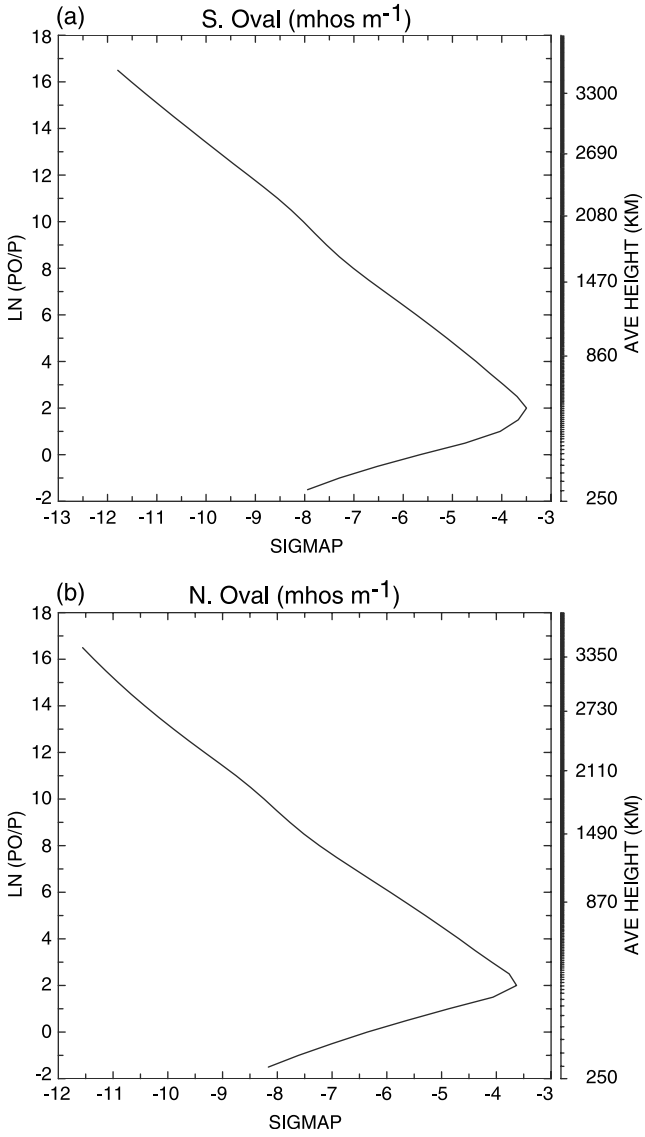

Figure 11. JTGCM Case 2 (auroral forcing plus scaled ion drag). Pedersen conductivity profiles are plotted in units of mhos m^{-1} for two locations: (a) within the south oval at 0° λ_{III} longitude and (b) within the north oval at 180° λ_{III} longitude. Two vertical scales are given: (1) log pressure, z = ln(p0/p), where z = 2 corresponds to 0.6-μbar, and (2) height (km).

two hemispheres is simulated. Zonal averaged and column integrated Pedersen conductivities in the southern oval region (up to 20.0 mhos) and northern oval region (up to 12.5 mhos) also reflect these hemispheric asymmetries (see above).

[66] Figure 12 illustrates both equatorial (2.5°N latitude; 0° λ_{III} longitude) and southern oval region (72.5°S latitude; 0° λ_{III} longitude) temperature profiles for Case 2. These specific locations are chosen to highlight the differences between auroral and nonauroral temperatures. Figure 13 quantifies the corresponding equatorial (Figure 13a) and southern auroral oval (Figure 13b) heat balances for these same locations. The former can be compared with Case 1 equatorial heat balances from Figure 7. The relatively "smooth" equatorial temperature profile in consistent with the fact that conduction dominates all the other cooling terms throughout most of the domain ($p \leq 5.0 \times 10^{-2}$ microbars). Furthermore, both horizontal advection and adiabatic heating terms dominate the Case 2 thermal balances below ~1000 km (pressures above 0.005-μbar); i.e., these dynamical terms reach 0.1 to 1.0 × 10^{-5} W/m^3 near the 1.0-μbar level. The magnitudes of these dynamical terms are much larger (by factors of 10–100) than for Case 1. This difference reflects the enhanced role of the intensified meridional circulation in both hemispheres as driven by strong Joule heating. When the specified equatorial drizzle is turned off, adiabatic heating and horizontal advection processes are still dominant and in control of the equatorial thermal budget. This strong dynamical heating is largely offset by H_3+ (2–4 micron) cooling above the CH_4 homopause, and hydrocarbon cooling below. Hence the strength of the meridional circulation is the key to the maintenance of the warm equatorial temperatures observed in the thermosphere of Jupiter, as also demonstrated by Majeed et al. (submitted manuscript, 2004).

[67] Figure 12 also shows that more "wiggles" occur in the southern oval temperature profile, since molecular conduction is not the dominant cooling term, except near the top of the JTGCM model domain. Specifically, Figure 13b illustrates that southern auroral oval temperatures are maintained by auroral heating above 800 km (pressures below 0.1-μbar), Joule heating over 400–1000 km (down to the 1.0 μbar level), and strong dynamical terms below the homopause. Corresponding cooling is provided by the strong upwelling winds (adiabatic cooling) plus conduction above 1750 km (pressures below 0.001-μbar), H_3+ (2–4 micron) cooling around the H_3+ ion peak, and strong hydrocarbon cooling below the homopause. At the lowest altitudes (below 400 km), local dynamical heating is strong (reaching 2.5–8.5 × 10^{-4} W/m^3) owing to the significant ion drag impact on the neutral wind pattern near the pole. At this southern oval location (0° λ_{III} longitude and 72.5°S latitude), Joule heating peaks at a higher altitude near

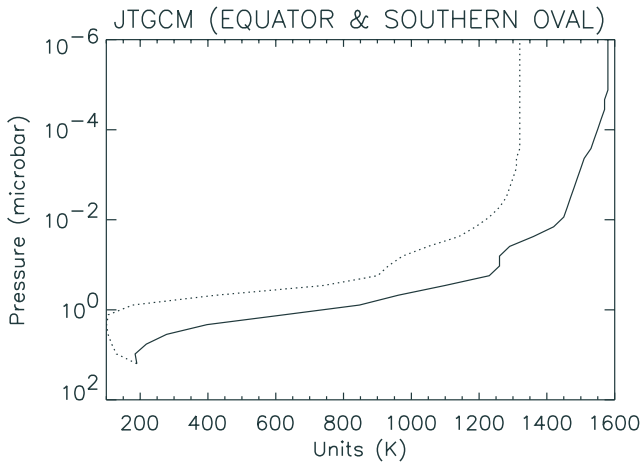

Figure 12. JTGCM Case 2 (auroral forcing plus scaled ion drag). Temperature profiles for equatorial (dotted curve) and south oval (solid curve) locations. These locations correspond to the heat balance plots of Figures 13a (equatorial) and 13b (south oval region), respectively.

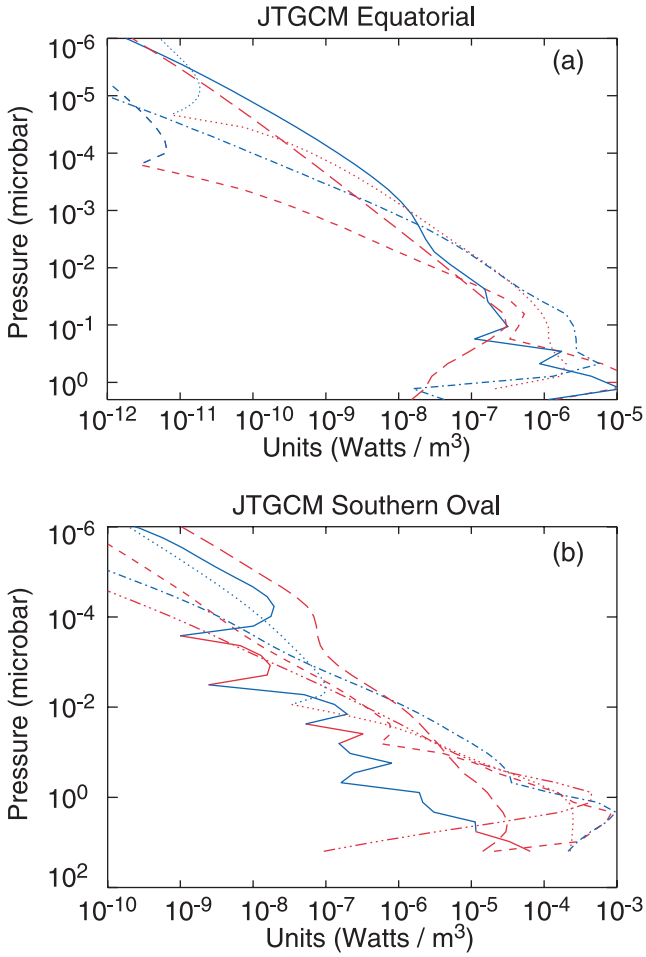

Figure 13. JTGCM Case 2 (auroral forcing plus scaled ion drag). Heat balance plots at (a) the equator and (b) the south oval region, comparing various terms as a function of pressure. IR cooling is derived from both hydrocarbon and H_3^+ (2–4 micron) emission. Red curve segments denote heating; blue curve segments denote cooling. Units are W/m^3. Individual curves are delineated as follows: (1) conduction (solid), (2) adiabatic heating/cooling (dotted), (3) IR cooling (dot-dashed), (4) drizzle heating (long dashed; equator only), (5) hydrodynamic advection (short-dashed), (6) auroral heating (long-dashed; polar only), and (7) Joule heating (3-dot dashed).

1.0 μbar at 4.5×10^{-4} W/m^3. Hence Joule heating is offset by both H_3+ and hydrocarbon cooling (at and above the homopause), while the strong dynamical heating below the homopause is regulated by hydrocarbon cooling alone. Furthermore, this southern oval location is primarily cooled by mechanisms other that conduction, for which "wiggles" in the temperature curve can be sustained.

[68] Zonally averaged heat balances (not shown) are important to describe in order to place the important hemispheric asymmetries in context. Joule heating is largest in the southern auroral oval region, peaking near 0.1-μbar at 2.0×10^{-6} W/m^3. The corresponding northern hemisphere Joule heating maximizes at the same pressure level at $\sim 7.0 \times 10^{-7}$ W/m^3. This factor of three asymmetry is significant and gives rise to the corresponding asymmetries in the zonal averaged wind fields above 0.1-μbar. Conversely, strong dynamical heating below the homopause at high southern latitudes (see Figure 13b) results from a combination of hydrodynamic advection and adiabatic heating terms. Zonally averaged values of both of these terms peak near 1.0-μbar at $\sim 1.0 \times 10^{-5}$ W/m^3. This strong heating is efficiently dissipated by hydrocarbon (mostly CH_4) cooling (see section 4).

[69] In summary, Case 2 illustrates a significantly modified Jovian thermospheric structure and global circulation compared to that calculated earlier for Case 1. In particular, the addition of scaled (30%) ion drag and Joule heating processes yields equatorial and polar temperatures that reasonably match available multispectral and Galileo ASI observations. These cases suggest that both auroral particle and Joule heating are required to simulate observed Jovian thermospheric temperatures. The underlying global thermospheric circulation is greatly intensified when ion drag and Joule heating processes are applied. The resulting strong neutral winds (up to 1.2 km/s) play a significant role in redistributing high-latitude heat and atomic hydrogen atoms toward the equator. Dynamical heating terms in fact are key to reproducing observed equatorial thermospheric temperatures; low-latitude ion precipitation has only a minor effect. A north-south asymmetry in the JTGCM circulation and temperature distribution is related to hemispheric differences in Pedersen conductivities and the ion drifts themselves. The reduced ion drag (30%) that is required suggests that (1) the convection electric field derived by Eviatar and Barbosa from Voyager may not be as strong at all magnetic longitudes, (2) improved JTGCM ionospheric densities are required that include a self-consistent formulation for H+, (3) there is inadequate vertical propagation of angular momentum from below the JTGCM boundary to provide a corotating lower boundary condition, and/or (4) there may exist uncertainties in the magnetosphere-ionosphere mapping that we have conducted using the VIP4 model. Overall, Case 2 provides a promising working model for which further JTGCM diagnostics can be derived enabling comparisons with available observations (see section 4). Brief comparisons with the JIM model are also warranted (see section 5).

3.3. Moderate Auroral Forcing Plus Full Ion Drag and Joule Heating

[70] Case 3 couples moderate auroral forcing (Case 1) plus 100% ion drag and Joule heating parameters to provide an "extreme" simulation for investigation. Here, the full Eviatar and Barbosa convection electric field is employed giving rise to large ion drifts (up to 3.0 km/s) whose impact on the thermospheric energetics and dynamics is examined. Recent Canada-France-Hawaii Telescope (CFHT) observations suggest that warm Jovian thermospheric temperatures in auroral "hot spots" (in excess of 1200 K) may occur occasionally [*Raynaud et al.*, 2004]. The present Case 3 simulation for these "extreme" conditions is not meant to be compared to the bulk of available multispectral and Galileo observations. Rather, this extreme case is useful to illustrate the impacts of very strong ion drag and Joule heating in the Jovian thermosphere. In addition, comparison of Case 2 and 3 zonal averaged fields is instructive.

[71] Zonal average slices of Case 3 temperature, wind, and composition fields are presented (see Figure 14) for

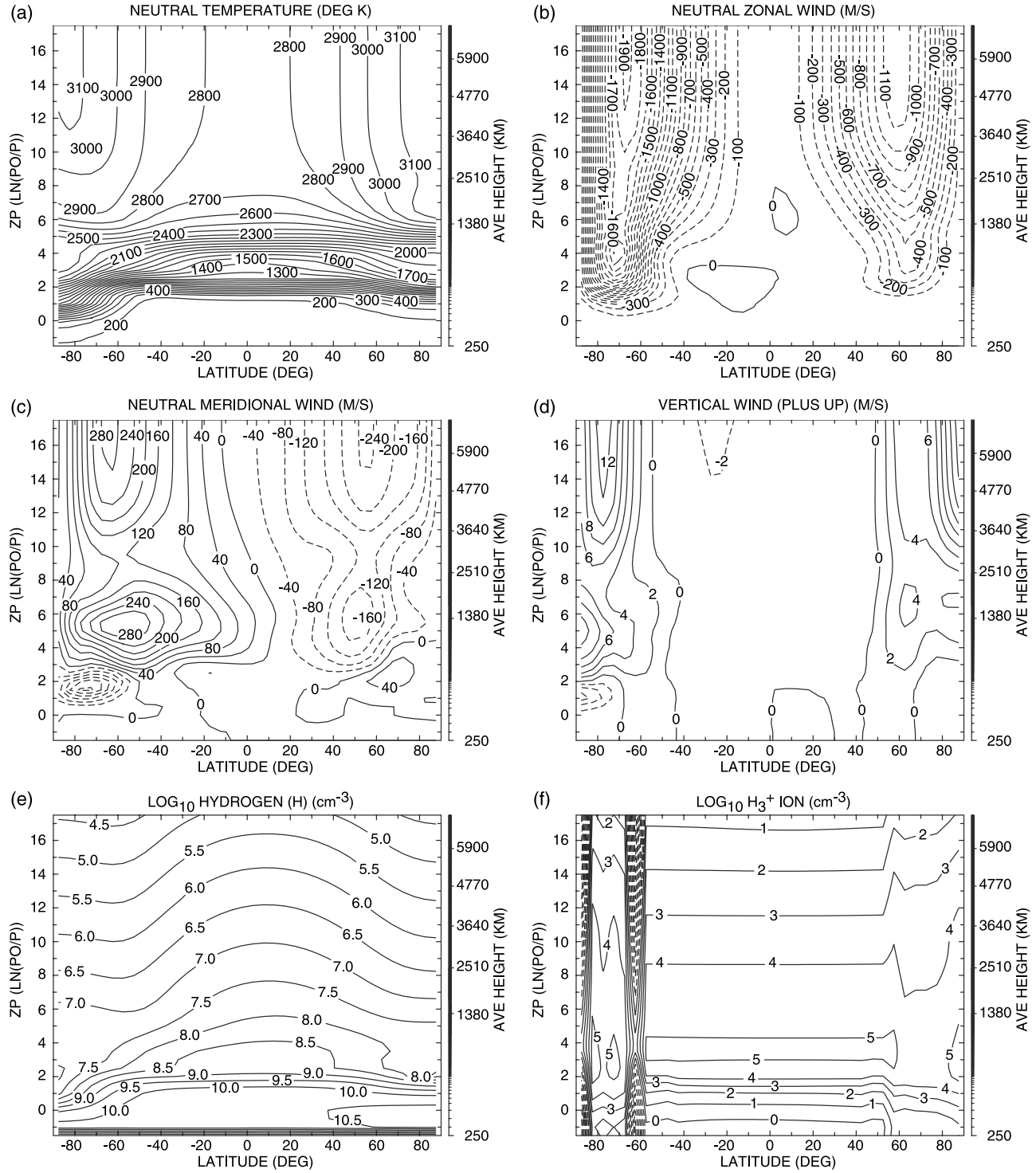

Figure 14. JTGCM Case 3 (auroral forcing plus full ion drag). Zonal average slices over the entire JTGCM vertical domain (in log pressure coordinates). Fields include (a) temperature (T) in 100 K intervals (200 to 3100 K); (b) neutral zonal winds (U) in 100 m/s intervals (−1900 to 0 m/s); (c) neutral meridional winds (V) in 40 m/s intervals (−240 to +280 m/s); (d) neutral vertical winds (W) in 2.0 m/s intervals (−6 to +16 m/s); (e) atomic hydrogen (H) in 0.5 intervals of $\log_{10}$ units (#/cm^3) (4.5 to 10.5); and (f) H_3^+ density in 1.0 intervals of $\log_{10}$ units (#/cm^3) (peaking at 2.5×10^5). Dashed lines indicate negative winds: zonal (westward), meridional (southward), and vertical (downward). Figure 14e and 14f densities ($\log_{10}$ #/cm^3) can be converted to $\log_{10}$ #/m^3 units by adding 6.0 to the contour intervals.

comparison to similar slices from Case 2 (Figure 10). These zonal average slices emphasize latitudinal variations. Clearly, the very strong Joule heating elevates topside thermospheric temperatures to 2800–3100 K (both ovals) and 2700–2800 K (near the equator). These values are 1400–1500 K warmer than simulated previously for Case 2. Temperatures near the 0.14-μbar level are also much warmer, approaching 1950–2450 K (ovals) and 1400 K (near the equator) for Case 3. Notice the strongest vertical temperature gradient appears near the equator over 1.0 to 0.05-μbar; temperatures rise by nearly 2000 K over this pressure region. Very strong dynamical heating (not shown), composed of adiabatic plus horizontal advection terms, gives rise to this strong equatorial warming. The intensified pole-to-equator circulation is ultimately responsible. Auroral oval temperatures are enormously enhanced by very strong Joule heating; i.e., zonally averaged peak heating is located near 0.1-μbar and approaches $\sim 1.0 \times 10^{-5}$ W/m^3 in the southern hemisphere. How do these extreme ion drag and Joule heating parameters impact the global circulation and the distribution of atomic species (e.g., hydrogen)?

[72] Figure 14b illustrates a deep and very strong zonal jet centered at 70°S latitude, with winds speeds reaching −1.9 km/s. This westward jet is largely driven by Joule heating in the southern oval region; initial equatorward driven winds are turned westward by the Coriolis torques. This jet dominates the southern hemisphere zonal flow, extends above the Jovian homopause throughout the thermosphere, and is consistent with strong meridional (equatorward) winds approaching +300 m/s (see Figure 14c). Both this strong zonal jet and the associated meridional wind speeds are more than double those previously calculated for Case 2. Immediately above the homopause at high southern latitudes, the westward zonal flow decreases dramatically, and is replaced by strong poleward (Figure 14c) and subsiding (Figure 14d) winds which produce strong dynamical heating at pressures above ∼1.0-μbar. In the northern hemisphere, the westward zonal jet is now centered at 60°N latitude, with winds speeds rising to −1.1 km/s (see Figure 14b); associated equatorward winds peak at −250 m/s (see Figure 14c). Corresponding vertical winds are strongly upward in the southern hemisphere (up to +12.0 m/s), downward at low latitudes (−2.0 m/s), and upward again near the north pole (up to +17.0 m/s) (see Figure 10d). Clearly, a strong zonally averaged circulation results from the added Joule heating, with upwelling/divergent winds at both poles, and convergent/downwelling flow near the equator. Maximum neutral horizontal winds (up to 2.3 km/s) are almost double those simulated for reduced ion-drag and Joule heating in Case 2. The intensified pole-to-equator global circulation plus the very warm thermospheric temperatures are clearly reflected in the hydrogen distribution (Figure 14e); i.e., pole-to-equator variations can be as large as a factor of ∼100 or more.

[73] In summary, very strong ion drag plus Joule heating processes implemented in the Case 3 simulation serve to (1) greatly strengthen the zonal, meridional, and vertical winds throughout the Jovian thermosphere, (2) strongly warm temperatures near 1000 km to values in excess of those inferred from observed H_3+ emissions, and (3) transport hydrogen atoms efficiently toward the equator. The Joule heating rates calculated are likely an upper limit to what is possible. Nevertheless, the Case 3 simulation demonstrates the capability of a strong global thermospheric circulation in redistributing heat and atomic species from the auroral oval regions toward lower latitudes. In particular, very warm equatorial temperatures are shown to be maintained by a balance of dynamical heating processes and H_3+ (2–4 micron) cooling above and hydrocarbon cooling below the CH_4 homopause.

4. JTGCM Diagnostics and Discussion

[74] Auroral (electron) precipitation, ion drag, and Joule heating processes together profoundly impact the simulated JTGCM global thermospheric circulation, and the underlying thermal and compositional distributions. Several diagnostics of these thermospheric features should be observable by ground-based or spacecraft platforms. We choose to investigate Case 2 diagnostic fields, since this case yields both auroral oval and equatorial temperatures that are reasonably consistent with available multispectral and Galileo ASI measurements.

[75] Figure 15a illustrates the atomic hydrogen distribution that results from this vigorous JTGCM thermospheric circulation. An integrated hydrogen column above the methane homopause is presented. This plot reveals a strong latitudinal gradient of hydrogen (a factor of 10–20), which increases from the south toward the north, in response to the stronger northward flow of the net global wind system. Equatorward winds are transporting atomic hydrogen from the northern and southern auroral oval source regions toward a "stagnation" point in the northern hemisphere, owing to the stronger net flow from south to north. Here, convergence of the horizontal winds occurs, and atomic hydrogen atoms "pile up," reaching a maximum column density of $\sim 2.6 \times 10^{17}$ cm^{-2}. The transport of hydrogen is efficient because its scale height is large with respect to helium and H_2. This Jovian interhemispheric hydrogen distribution does not display an equatorial "bulge," in part due to prescribed JTGCM auroral forcing that is symmetric in λ_{III} longitude. However, other forces that are asymmetric in λ_{III} longitude, and under magnetic control, may act to further steer the neutral thermospheric circulation thereby focusing the hydrogen atoms toward specific longitudes as observed [e.g., *McGrath*, 1991]. Moreover, any north-south asymmetry in the hydrogen distribution should be reflected in the observed Lyman-α emission, which can serve as a tracer of the Jovian thermospheric circulation.

[76] The total heating simulated in both auroral oval regions should also be reflected in the corresponding total cooling that results from its dissipation. Table 3 summarizes zonal averaged column integrated thermal balances in the northern and southern oval regions. Values are selected for interhemispheric comparison at ±70° latitude above ∼400 km, at pressures less than 1.5-μbar where steady state conditions largely prevail. Units of mW/m^2 are displayed to provide consistency with volume heating and cooling rates (units of mW/m^3) illustrated in Figures 2, 7, and 13. Large Joule heating rates for Case 2 are calculated to be 70 mW/m^2 in the northern oval region, and nearly double (up to ∼140 mW/m^2) in the southern auroral oval (see Table 3). Auroral particle heating, when zonally averaged, contributes up to 8.5 mW/m^2 to the southern

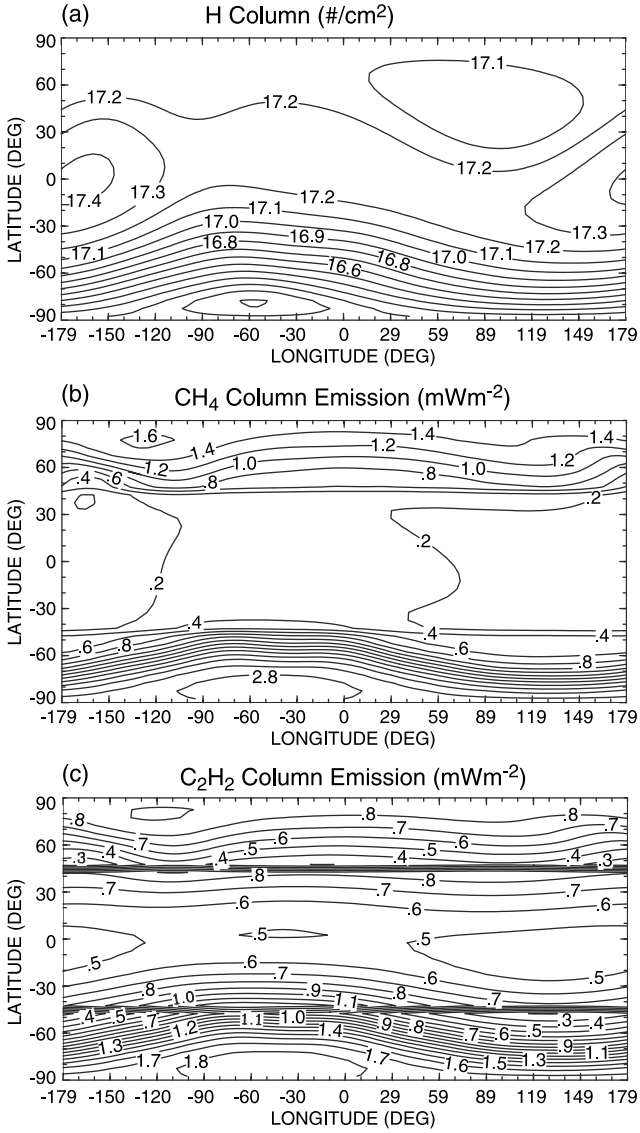

Figure 15. JTGCM Case 2 (auroral forcing plus scaled ion drag). Diagnostic plots are shown for column integrated quantities in order to provide observers with JTGCM predictions that can be tested. Quantities include (a) atomic hydrogen (in $\log_{10}$ #/cm^2 units), (b) hydrocarbon (CH_4 7.8-micron) cooling (in $\log_{10}$ mW/m^2 units), and (c) hydrocarbon (C_2H_2 13.4-micron) cooling (in $\log_{10}$ mW/m^2 units). The column of atomic hydrogen is calculated above the CH_4 homopause; the hydrocarbon cooling columns are integrated throughout the entire JTGCM domain (above 250 km). Figure 15a column densities are given in $\log_{10}$ #/cm^2 units to facilitate comparison with Figure 10e; conversion to $\log_{10}$ #/m^2 units is accomplished by adding 4.0 to the contour intervals.

oval region. IR cooling plus dynamical cooling combine to generally balance this auroral plus Joule heating (within ±30%) in both hemispheres. Column integrated IR cooling rates, above the CH_4 homopause, are larger in the southern hemisphere (85 mW/m^2) than in the north (17.5 mW/m^2). Dynamical cooling is also important (110 mW/m^2) in the southern hemisphere. Recall that the hemispheric asymmetry in these Joule heating rates is due to a number of factors: (1) consistently larger ion drifts in the southern oval region, (2) differences in VIP4 magnetic field topologies of the northern and southern oval regions, and (3) hemispheric differences in the Pedersen conductivities (see section 3.2).

[77] It is noteworthy that H_3^+ (2–4 micron) emission contributes to cooling of auroral region thermospheric temperatures far above the CH_4 homopause to rather low pressures. This IR cooling increases as the local H_3^+ densities increase, in response to the specified auroral oval (electron) precipitation (see section 2.6). The associated oval heating is partially regulated by this variable H_3^+ cooling. Column integrated H_3^+ densities maximize in the southern auroral oval region (not shown), reaching $\sim 4.0 \times 10^{16}$ m^{-2}. The corresponding column integrated H_3^+ cooling rate approaches nearly 2.0 mW/m^2. For the northern oval region, column densities are reduced somewhat ($\sim 3.0 \times 10^{16}$ m^{-2}), with appropriately smaller cooling rates ($\sim$1.5 mW/m^2). Thus H_3^+ cooling acts as a thermostat regulating Jovian upper thermosphere temperatures which are subject to soft electron precipitation and Joule heating (see section 2.6).

[78] Thermal balances below the CH_4 homopause are not captured by the entries in Table 3. Strong dynamical heating in the southern oval region is of greatest importance; warming results from adiabatic heating and lateral advection associated with strong poleward and subsiding flow (see Figures 10c and 10d), reaching nearly 800 mW/m^2. Figures 15b and 15c illustrate CH_4 (7.8-micron) and C_2H_2 (13.4-micron) column integrated cooling rates (in mW/m^2) throughout the entire JTGCM domain. Total IR cooling is strongest in the southern hemisphere (up to 810 mW/m^2 from CH_4 and 73 mW/m^2 from C_2H_2 emission). The bulk of this strong IR cooling (about 800 mW/m^2) serves to balance the strong dynamical heating poleward of the auroral oval. Conversely, the northern oval region exhibits much weaker CH_4 cooling ($\sim$40 mW/m^2) and C_2H_2 cooling ($\sim$10 mW/m^2), since dynamical heating below the homopause is minimal in the northern oval region. Thus it is clear that hydrocarbon cooling is an effective sink of heat deposited near/below the homopause.

[79] Are the JTGCM (Case 2) column integrated cooling rates summarized in Figures 15b and 15c reasonable? *Drossart et al.* [1993] reviewed observed IR emission rates from the northern auroral region using Voyager Infrared Interferometer and Radiometer Spectrometer (IRIS) data. The strongest emissions are observed in the northern auroral

Table 3. Column Thermal Balances: Case 2[a]

Agent	North Oval	South Oval
Joule Heating	70.0	140.0
Auroral Heating	1.75	8.5
Dynamical Cooling	−35.0	−110.0
Total IR Cooling	−17.5	−85.0
Net Heating	19.25	−46.5
IR Cooling Terms		
CH_4 Cooling	−13.5	−68.0
C_2H_2 Cooling	−1.0	−2.0
H_3+ Cooling	−3.0	−15.0
Total IR Cooling	−17.5	−85.0

[a]Units: mW/m^2.

region, but it is difficult to view the poles from equatorial observations. Strong hydrocarbon emissions from northern auroral "hot spots" are likely the result of both localized particle precipitation plus Joule heating. The former can be estimated from the energy influx from particle precipitation inferred from Voyager UVS observations [e.g., *Herbert et al.*, 1987]. The contribution from Joule heating is largely unconstrained, but is estimated from scaling arguments to be as much as 50% of the total IR emission. Drossart et al. estimate the integrated excess IR emission over the global IRIS field of view to be 208±15 mW/m^2, composed mostly of CH_4 and C_2H_2 emission. Maximum IR cooling rates from the JTGCM northern auroral region are much smaller ($\sim$50 mW/m^2) than those inferred from IRIS observations. This is reasonable, since the Case 2 JTGCM simulation does not incorporate intense particle precipitation appropriate to a localized auroral "hot spot."

[80] Conversely, JTGCM hydrocarbon cooling rates (Case 2) in the southern hemisphere are calculated to be nearly 880 mW/m^2, as required to balance strong dynamical heating (up to 800 mW/m^2) below the homopause. This cooling rate is much larger than the IRIS value of 208 ± 15 mW/m^2 corresponding to an auroral "hot spot." However, the JTGCM zonal averaged Joule heating rate of $\sim$140 mW/m^2 is similar to that estimated from Drossart et al. from scaling arguments. We conclude that a straightforward comparison of southern hemisphere cooling rates from the JTGCM with IRIS observations is not possible until steady state conditions are obtained within the JTGCM below 400 km.

[81] Recent H_3^+ emission rates and column densities [e.g., *Stallard et al.*, 2002] indicate that variations across the auroral oval can be as much as a factor of 6. A maximum emission of 3.1 mW/m^2 was observed, corresponding to an H_3^+ column density of 1.4×10^{16} m^{-2}. Case 2 JTGCM values (above) are comparable for both the southern and northern oval regions. The corresponding JTGCM topside temperatures of 1500–1600 K are maintained by a balance of auroral particle heating, H_3+ emission and thermal conduction. The simulated JTGCM H_3^+ emission rates are very similar, suggesting that the simulated JTGCM temperatures are reasonable as well.

5. Initial Comparisons of JTGCM and JIM Simulations

[82] A good summary of the JIM model and key simulations is given by *Millward et al.* [2002]. Recently, a suite of JIM model simulations was conducted to investigate how ionospheric densities and conductivities respond to variations in electron precipitation within the auroral ovals. The goal was to study the effects of fluxes of auroral electrons on the neutral and ion structure. These runs utilized different electrons with an assumed initial energy (E_0) of 10 keV and energy fluxes (E_f) ranging from 0.1 to 1000 mW m^{-2}. Recall that the JTGCM prescribes electron precipitation with energies (E_0) distributed among three components: (1) 22 keV particles (100 mW m^{-2}), (2) 3 keV particles (10 mW m^{-2}), and (3) 100 eV particles (0.5 mW m^{-2}), yielding a total auroral energy flux of $\sim$110 mW m^{-2}. The 22 keV component clearly deposits its energy near the homopause. Our JTGCM prescription for auroral electron precipitation most closely corresponds to the JIM case for which E_0 = 100 mW m^{-2} and E_f = 10 keV. However, it is anticipated that JTGCM electrons (22 keV) will deposit their energy at higher pressures (lower altitudes) than JIM particles (10 keV) for the same energy flux ($\sim$100 mW m^{-2}).

[83] We utilize selected JTGCM oval locations (north: 180° λ_{III}, 57.5°N; south: 0° λ_{III}, 72.5°S) to extract H_3^+ profiles and column densities, and column integrated Pedersen conductivities for comparison to corresponding JIM values [*Millward et al.*, 2002]. The 10 keV electrons from JIM produce an auroral H_3^+ profile having a peak of $\sim 1.0 \times 10^{12}$ m^{-3} at 0.1-μbar (near 700 km). The corresponding JIM H_3^+ column densities approach 2.0×10^{17} m^{-2}, with an integrated Pedersen conductivity of about 1.0 mhos [*Millward et al.*, 2002]. For the northern oval, a JTGCM peak H_3^+ density of $\sim 3.8 \times 10^{11}$ m^{-3} appears at 0.22-μbar (near 550–600 km), which indeed occurs deeper and at higher pressure than the JIM simulation. The associated JTGCM H_3^+ column density approaches 3.8×10^{16} m^{-2}, and yields an integrated Pedersen conductivity of about 9 mhos. This conductivity is nearly a factor of 10 larger than calculated by the JIM model. On the other hand, for the southern oval, a JTGCM peak H_3^+ density of $\sim 4.4 \times 10^{11}$ m^{-3} again appears at 0.22-μbar, but now at a higher altitude near 700 km (owing to warmer temperatures). The corresponding JTGCM H_3^+ column density approaches 4.4×10^{16} m^{-2}, and yields an integrated Pedersen conductivity of about 12.5 mhos. These JIM and JTGCM differences in H_3^+ peak (and column integrated) densities may be due to the deeper penetration of the JTGCM H_3^+ peak, for which the reaction with CH_4 is more efficient (see Table 2). In addition, some of the discrepancy among Pedersen conductivities may result from the use of different magnetic field models to compute conductivities within the JIM and JTGCM codes.

[84] Overall, these initial JIM and JTGCM comparisons reveal that (1) auroral particle heating and H_3^+ ion production are different for these independent prescriptions for auroral electron precipitation and (2) the VIP4 magnetic field model produces different values for simulated conductivities. Detailed JIM and JTGCM comparisons require a comprehensive campaign for which a common suite of auroral and ion drag inputs are incorporated for benchmark simulations. These JIM and JTGCM simulations must be integrated to steady state, in excess of 40–60 Jovian rotations, for useful comparisons to be conducted.

6. Summary and Conclusions

[85] A fully 3-D Jupiter Thermospheric General Circulation Model (JTGCM) was developed and exercised to address global temperatures, three-component neutral winds, and neutral-ion specie distributions from $\sim$250 to 3000 km. Our goal is to reproduce available multispectral and in situ measurements of the Jovian thermosphere-ionosphere system and to understand the underlying processes that maintain and drive enormous variations in this structure.

[86] Results from three JTGCM cases are presented which incorporate moderate auroral heating, moderate ion drag and Joule heating rates, and large ion drag and Joule heating. The best JTGCM simulation requires a $\sim$30%

scaling of ion drag and Joule heating parameters (from the estimated maximum) in order to simulate equatorial and polar temperatures that reasonably match available multispectral and Galileo ASI observations. This case suggests that both auroral particle and Joule heating are required to simulate observed Jovian thermospheric temperatures and densities at both low and high latitudes above the homopause. The underlying global thermospheric circulation is greatly intensified when ion drag and Joule heating processes are applied to an otherwise aurorally driven wind system. The resulting strong neutral winds (up to 1.2 km/s) play a significant role in redistributing high-latitude heat and atomic hydrogen atoms toward the equator. Dynamical heating terms in fact are key to reproducing observed equatorial thermospheric temperatures; ion precipitation has only a minor effect. A north-south asymmetry exists in the JTGCM circulation and temperature distribution, which is related to hemispheric differences in Pedersen conductivities and the ion drifts themselves. The reduced ion drag (30%) that is required may imply (1) the convection electric field derived by Eviatar and Barbosa from Voyager may not be as strong at all magnetic longitudes, (2) improved JTGCM ionospheric (H+) densities are required, (3) there is inadequate vertical propagation of angular momentum from below the JTGCM lower boundary, and/or (4) there exist uncertainties in the magnetosphere-ionosphere mapping that we have conducted using the VIP4 model. Overall, it is clear that the variability of Jupiter's thermospheric structure and dynamics is likely triggered and regulated by this magnetosphere-ionosphere coupling.

[87] The present JTGCM code yields a realistic working model for which further detailed comparisons with available observations and the JIM model are warranted. Detailed JIM and JTGCM comparisons require a comprehensive campaign for which a common suite of auroral and ion drag inputs are incorporated for benchmark simulations. These JIM and JTGCM simulations must be integrated to steady state, in excess of 40–60 Jovian rotations, for useful studies to be done.

[88] Future upgrades to the JTGCM code are planned to improve the self-consistency of the energetic, dynamical, and chemical processes so that magnetic storm events and the time variable responses of the Jovian thermosphere and ionosphere can be captured and studied in detail. For instance, new formulations for H^+ ionospheric diffusion and explicit H^+ losses via H_2-vibrational states will be incorporated. In addition, solar EUV production terms for neutral and ion species will be calculated explicitly throughout a Jovian rotation. JTGCM auroral forcing will be enhanced to include asymmetries in λ_{III} longitude; this is required to focus hydrogen transport from the auroral oval regions toward the equator where an atomic-H bulge may form. Furthermore, the magnetosphere-ionosphere coupling and the resulting ion convection pattern are over-simplified within the present JTGCM code. Future effort will be made to improve the VIP4 magnetic field model mapping of the Jovian magnetosphere to the ionosphere. Improved ion momentum drag and Joule heating rates will then be available for use in future JTGCM simulations. Finally, the impact of upward propagating waves, including tides and gravity waves, remains to be addressed.

[89] **Acknowledgments.** We are grateful to the National Center for Atmospheric Research (NCAR) for the use of the IBM/SP and SGI supercomputer resources necessary to develop and exercise the JTGCM thermospheric model and its postprocessor. In addition, special thanks go to Ben Foster of NCAR for his help preparing the JTGCM code to run on the IBM/SP computers. Finally, we wish to thank Denis Grodent for the use of his multicomponent Jovian auroral heating formulation.

References

Achilleos, N., S. Miller, J. Tennyson, A. D. Aylward, I. Mueller-Wodarg, and D. Rees (1998), JIM: A time-dependent, three-dimensional model of Jupiter's thermosphere and ionosphere, *J. Geophys. Res.*, *103*(E9), 20,089–20,112.

Atreya, S. K. (1986), *Atmospheres and Ionospheres of the Outer Planets and Their Satellites*, Springer, New York.

Banks, P. M., and G. Kockarts (1973), *Aeronomy*, Elsevier, New York.

Bates, D. R., M. F. Guest, and R. A. Kendall (1993), Enigma of H_3^+ dissociative recombination, *Planet. Space Sci.*, *41*, 9–15.

Bougher, S. W., R. E. Dickinson, E. C. Ridley, and R. G. Roble (1988), Venus mesosphere and thermosphere III. Three-dimensional general circulation with coupled dynamics and composition, *Icarus*, *73*, 545–573.

Bougher, S. W., S. Engel, R. G. Roble, and B. Foster (1999), Comparative terrestrial planet thermospheres: 2. Solar cycle variation of global structure and winds at equinox, *J. Geophys. Res.*, *104*, 16,591–16,611.

Bougher, S. W., S. Engel, R. G. Roble, and B. Foster (2000), Comparative terrestrial planet thermospheres: 3. Solar cycle variation of global structure and winds at solstices, *J. Geophys. Res.*, *105*, 17,669–17,689.

Bougher, S. W., et al. (2002), Simulations of the upper atmospheres of the terrestrial planets, in *Atmospheres in the Solar System: Comparative Aeronomy*, *Geophys. Monogr. Ser.*, vol. 130, edited by M. Mendillo, A. Nagy, and H. Waite, pp. 261–288, AGU, Washington, D. C.

Chapman, S., and T. G. Cowling (1970), *The Mathematical Theory of Non-uniform Gases*, 423 pp., Cambridge Univ. Press, New York.

Clarke, J. T., Jr., L. B. Jaffel, and J. Gérard (1998), Hubble Space Telescope imaging of Jupiter's UV aurora during the Galileo orbiter mission, *J. Geophys. Res.*, *103*(E9), 20,217–20,236.

Connerney, J. E. P., M. H. Acuña, N. F. Ness, and T. Satoh (1998), New models of Jupiter's magnetic field constrained by the Io flux tube footprint, *J. Geophys. Res.*, *103*(A6), 11,929–11,940.

Cowley, S. W. H., and E. J. Bunce (2001), Origin of the main auroral oval in Jupiter's coupled magnetosphere-ionosphere system, *Planet. Space Sci.*, *49*, 1067–1088.

Cravens, T. E. (1987), Vibrationally excited molecular hydrogen in the upper atmosphere of Jupiter, *J. Geophys. Res.*, *92*, 11,083–11,100.

Dessler, A. J. (1983), Appendix B: Coordinate Systems, in *Physics of the Jovian Magnetosphere*, pp. 498–504, Cambridge Univ. Press, New York.

Drossart, P., et al. (1989), Detection of H_3^+ on Jupiter, *Nature*, *340*, 539–542.

Drossart, P., B. Bézard, S. K. Atreya, J. Bishop, J. H. Waite Jr., and D. Boice (1993), Thermal profiles in the auroral regions of Jupiter, *J. Geophys. Res.*, *98*(E10), 18,803–18,812.

Eviatar, A., and A. D. Barbosa (1984), Jovian magnetospheric neutral wind and auroral precipitation flux, *J. Geophys. Res.*, *89*, 7393–7398.

Festou, M. C., S. K. Atreya, T. M. Donahue, B. R. Sandel, D. E. Shemansky, and A. L. Broadfoot (1981), Composition and thermal profiles of the Jovian upper atmosphere determined by the Voyager stellar occultation experiment, *J. Geophys. Res.*, *86*, 5715–5735.

Flasar, F. M., et al. (2004), An intense stratospheric jet on Jupiter, *Nature*, *427*, 132–135.

Gladstone, G. R., M. Allen, and Y. L. Yung (1996), Hydrocarbon photochemistry in the upper atmosphere of Jupiter, *Icarus*, *119*, 1–52.

Gladstone, G. R., et al. (2002), A pulsating auroral x-ray hot spot on Jupiter, *Nature*, *415*(6875), 1000–1003.

Grodent, D., Jr., and J. Gérard (2001), A self-consistent model of the Jovian auroral thermal structure, *J. Geophys. Res.*, *106*(A7), 12,933–12,952.

Grodent, D., J. T. Clarke, J. Kim, J. H. Waite Jr., and S. W. H. Cowley (2003), Jupiter's main auroral oval observed with HST-STIS, *J. Geophys. Res.*, *108*(A11), 1389, doi:10.1029/2003JA009921.

Herbert, F., B. R. Sandel, and A. L. Broadfoot (1987), Observations of the Jovian UV aurora by Voyager, *J. Geophys. Res.*, *92*, 3141–3154.

Hickey, M. P., R. L. Walterscheid, and G. Schubert (2000), Gravity wave heating and cooling in Jupiter's thermosphere, *Icarus*, *148*, 266–281.

Hill, T. W. (1979), Inertial limit of co-rotation, *J. Geophys. Res.*, *84*, 6554–6558.

Hill, T. W. (2001), The Jovian auroral oval, *J. Geophys. Res.*, *106*, 8101–8107.

Kim, Y. H., and J. L. Fox (1994), The chemistry of hydrocarbon ions in the Jovian ionosphere, *Icarus*, *112*, 310–325.

Lam, H. A., et al. (1997), A baseline spectroscopic study of the infrared auroras of Jupiter, *Icarus*, *127*, 379–393.

Larsson, M. (1997), Dissociative recombination with ion storage rings, *Annu. Rev. Phys. Chem.*, *48*, 151–179.
Lide, D. R. (Ed.) (1997), *CRC Handbook of Chemistry and Physics*, 78th ed., CRC Press, Boca Raton, Fla.
Majeed, T., and J. C. McConnell (1991), The upper ionospheres of Jupiter and Saturn, *Planet. Space Sci.*, *39*, 1715–1732.
Mason, E. A., and T. R. Marrero (1970), The diffusion of atoms and molecules, *Adv. Mol. Phys*, *6*, 156–232.
Matcheva, K. I., and D. F. Strobel (1999), Heating of Jupiter's thermosphere by dissipation of gravity waves due to molecular viscosity and heat conduction, *Icarus*, *140*, 328–340.
McGrath, M. A. (1991), An unusual change in the Jovian Lyman-α bulge, *Geophys. Res. Lett.*, *18*, 1931–1934.
Miller, S., R. D. Joseph, and J. Tennyson (1990), Infrared emissions of H_3^+ in the atmosphere of Jupiter in the 2.1 and 4.0 micron region, *Astrophys. J.*, *360*, L55–L58.
Miller, S., et al. (1997), Mid-to-low latitude H_3^+ emission from Jupiter, *Icarus*, *130*, 57–67.
Millward, G. H., et al. (2002), Thermospheric general circulation models for the giant planets: The Jupiter case, in *Atmospheres in the Solar System: Comparative Aeronomy*, *Geophys. Monogr. Ser.*, vol. 130, edited by M. Mendillo, A. Nagy, and H. Waite, pp. 289–298, AGU, Washington, D. C.
Mitchell, J. B., et al. (1983), Measurements of the branching ratio for the dissociative recombination of H_3^+ + e, *Phys. Rev. Lett.*, *51*, 885–888.
Moses, J. I., and S. F. Bass (2000), The effects of external material on the chemistry and structure of Saturn's ionosphere, *J. Geophys. Res.*, *105*(E3), 7013–7052.
Niemann, H. B., et al. (1996), The Galileo Probe Mass Spectrometer: Composition of Jupiter's atmosphere, *Science*, *272*, 846–849.
Raynaud, E., et al. (2004), Spectro-imaging observations of Jupiter's 2-micron auroral emission. I. H_3 + distribution and temperature, *Icarus*, *171*, 133–152.
Rego, D., et al. (1999), Supersonic winds in Jupiter's aurorae, *Nature*, *399*, 121–124.
Richmond, A. D., E. C. Ridley, and R. G. Roble (1992), A thermosphere/ionosphere general circulation model with coupled electrodynamics, *Geophys. Res. Lett.*, *19*, 601–604.
Robert, A. J. (1966), The integration of a low order spectral form of the primitive meteorological equations, *J. Meteorol. Soc. Jpn.*, *44*, 237–245.
Roble, R. G., and E. C. Ridley (1987), An auroral model for the NCAR thermospheric general circulation model (TGCM), *Ann. Geophys., Ser. A*, *5*(6), 369–382.
Roble, R. G., E. C. Ridley, A. D. Richmond, and R. E. Dickinson (1988), A coupled thermospheric-ionospheric general circulation model, *Geophys. Res. Lett.*, *15*, 1325–1328.
Seiff, A., D. B. Kirk, T. C. D. Knight, R. E. Young, J. D. Mihalov, L. A. Young, F. S. Milos, G. Schubert, R. C. Blanchard, and D. Atkinson (1998), Thermal structure of Jupiter's atmosphere near the edge of a 5-μm hot spot in the north equatorial belt, *J. Geophys. Res.*, *103*(E10), 22,857–22,890.
Sommeria, J., L. Ben-Jaffel, and R. Prange (1995), On the existence of supersonic jets in the upper atmosphere of Jupiter, *Icarus*, *119*, 2–25.
Stallard, T. S., S. Miller, G. Millward, and R. D. Joseph (2001), On the dynamics of the Jovian ionosphere: I. The measurement of ion winds, *Icarus*, *154*, 475–491.
Stallard, T. S., S. Miller, G. Millward, and R. D. Joseph (2002), On the dynamics of the Jovian ionosphere: II. The measurement of H_3^+ vibrational temperature, column density and total emission, *Icarus*, *156*, 498–514.
Strobel, D. F. (2002), Aeronomic systems on planets, moons, and comets, in *Atmospheres in the Solar System: Comparative Aeronomy*, *Geophys. Monogr. Ser.*, vol. 130, edited by M. Mendillo, A. Nagy, and H. Waite, pp. 7–22, AGU, Washington, D. C.
Strobel, D. F., and G. R. Smith (1973), On the temperature of the Jovian thermosphere, *J. Atmos. Sci.*, *30*, 718–725.
Sundstrom, G., et al. (1994), Destruction rate of H_3+ by low-energy electrons measured in a storage-ring experiment, *Science*, *263*, 785–787.
Waite, J. H., Jr., and D. Lummerzheim (2002), Comparison of auroral processes: Earth and Jupiter, in *Atmospheres in the Solar System: Comparative Aeronomy*, *Geophys. Monogr. Ser.*, vol. 130, edited by M. Mendillo, A. F. Nagy, and J. H. Waite, pp. 115–139, AGU, Washington, D. C.
Waite, J. H., Jr., T. E. Cravens, J. U. Kozyra, A. F. Nagy, S. K. Atreya, and R. H. Chen (1983), Electron precipitation and related aeronomy of the Jovian thermosphere and ionosphere, *J. Geophys. Res.*, *88*, 6143–6163.
Waite, J. H., Jr., G. R. Gladstone, W. S. Lewis, P. Drossart, T. E. Cravens, A. N. Maurellis, B. H. Mauk, and S. Miller (1997), Equatorial X-ray emissions: Implications for Jupiter's high exospheric temperatures, *Science*, *276*, 104–108.
Waite, J. H., et al. (2000), Multispectral observations of Jupiter's aurora, *Adv. Space Res.*, *26*, 1453–1475.
Waite, J. H., Jr., et al. (2001), An auroral flare at Jupiter, *Nature*, *410*, 787–789.
Yelle, R. V., and S. Miller (2004), Jupiter's thermosphere and ionosphere, in *Jupiter: The Planet, Satellites, and Magnetosphere*, edited by F. Bagenal, T. E. Dowling, and W. B. McKinnon, chap. 9, pp. 185–218, Cambridge Univ. Press, New York.
Yelle, R. V., L. A. Young, R. E. Young, A. Sieff, and D. B. Kirk (1996), Structure of Jupiter's upper atmosphere: Prediction for Galileo, *J. Geophys. Res.*, *101*, 2149–2162.
Young, L. A., R. V. Yelle, R. Young, A. Sieff, and D. B. Kirk (1997), Gravity waves in Jupiter's thermosphere, *Science*, *276*, 108–111.

S. W. Bougher, T. Majeed, and J. H. Waite Jr., Space Physics Research Laboratory, University of Michigan, Ann Arbor, MI 48109-2143, USA. (bougher@umich.edu; tariqm@umich.edu; hunterw@umich.edu)
G. R. Gladstone, Southwest Research Institute, San Antonio, TX 78228-0510, USA. (randy@whistler.space.swri.edu)